

Hybrid quantum algorithms for flow problems

Sachin S. Bharadwaj^{1,*} and Katepalli R. Sreenivasan^{1, 2, 3, 4, †}

¹*Department of Mechanical and Aerospace Engineering, New York University, New York 11201 USA*

²*Courant Institute of Mathematical Sciences, New York University, New York, NY 10012*

³*Department of Physics, New York University, New York, NY 10012*

⁴*Center for Space Science, New York University Abu Dhabi, Abu Dhabi 129188, United Arab Emirates*

(Dated: July 4, 2023)

For quantum computing (QC) to emerge as a practically indispensable computational tool, the exigency is for quantum protocols with an end-to-end practical applications—in this instance, fluid dynamics. To facilitate this, we debut here a high performance quantum simulator which we term *QFlowS* (Quantum Flow Simulator), designed for fluid flow simulations using QC. Solving nonlinear flows by QC generally proceeds by solving an equivalent infinite dimensional linear system as a result of linear embedding. Thus, we first choose to simulate two well known linear, unsteady flows using *QFlowS* and demonstrate a previously unseen, full gate-level implementation of a hybrid and high precision Quantum Linear Systems Algorithms (QLSA) for simulating such flows. The utility of this simulator is shown by extracting error estimates and a power law scaling that relates T_0 (a parameter crucial to Hamiltonian simulations) to the condition number κ of the simulations matrix, and allows the prediction of an optimal scaling parameter for accurate eigenvalue estimation. Further, we append two speedup preserving algorithms for (a) the functional form or sparse quantum state preparation and (b) *in situ* quantum post-processing to compute a nonlinear function of the velocity field, namely the the viscous dissipation rate, resulting in an end-to-end complexity of $\mathcal{O}(\text{poly log}(N/\epsilon)\kappa/\epsilon_{QPP})$, where N is the size of the linear system of equations, ϵ is the accuracy of the solution and ϵ_{QPP} is the accuracy of post processing. This work demonstrates a possible way towards quantum simulation of fluid flows, and highlights the special considerations needed at the gate level implementation of QC.

I. INTRODUCTION

Computer simulations of nonlinear physical systems—such as turbulent flows, glassy systems, climate physics, molecular dynamics and protein folding—are formidably hard to perform on even the most powerful supercomputers of today or of foreseeable future. In particular, the state-of-the-art Direct Numerical Simulations (DNS) of turbulent flows [1–3] governed by the Navier-Stokes equations, or of turbulent reacting flow problems and combustion [4], both of which involve massive simulations with high grid resolutions, not only reveal fine details of the flow physics [5, 6], but also constantly contend with the limits of supercomputers on which the codes run [7]. However, simulation sizes required to settle fundamental asymptotic theories, or simulate turbulent systems such as the Sun or cyclones, or to simulate flows around complex geometries of practical interest, would require computing power that is several orders of magnitude higher than is currently available. Reaching such computational prospects calls for a paradigm shift in the computing technology.

One such potential candidate is Quantum Computing (QC)[8], which has striven to establish its advantage over classical counterparts by promising polynomial or exponential speedups [9]. Even though QC has been around for the last two decades, the subject is still nascent. In

this nascent era, which has been called the Noisy Intermediate Scale Quantum (NISQ) era, QC’s applications already extend [10, 11] across finance, chemistry, biology, communication and cryptography, but not as much in areas that are predominantly nonlinear, such as fluid dynamics.

This work attempts to pave the way for utilizing QC in Computational Fluid Dynamics (CFD) research, which we have termed [12] Quantum Computation of Fluid Dynamics (QCFD). An initial comprehensive survey of various possible directions of QCFD was made in [12]. Realistic CFD simulations with quantum advantages require one to quantumly solve general nonlinear PDEs such as the Navier-Stokes equations. However, it is worth noting that the fundamental linearity of quantum mechanics itself blockades encoding of nonlinear terms, thus forcing a linearization of some kind [13–15], which typically results in an *infinite* dimensional linear system. In such cases the inaccessibility to the required large number of qubits (and thus exponentially large vector spaces) leads to inevitable truncation errors, limiting the focus to weakly nonlinear problems [13]. Therefore the ability to solve high dimensional linear systems in an end-to-end manner [16] while capturing the flow physics is crucial to simulating nonlinear flow problems. Our goal here is to present various steps involved in the process of solving simple and idealized problems, including providing estimates of scaling and errors involved.

To this end, we unveil here a high performance quantum simulator which we call *QFlowS*(Quantum Flow Simulator), designed particularly to simulate fluid flows. Built on a C++ platform, it offers both QC and CFD

* sachin.bharadwaj@nyu.edu

† katepalli.sreenivasan@nyu.edu

tools in one place. With QFlowS we implement a modified version of the class of algorithms, now termed Quantum Linear Systems Algorithms (QLSA). Under some caveats, these algorithms promise to solve a linear system of equations given by the matrix inversion problem $A\mathbf{x} = \mathbf{b}$, with up to an exponential speedup compared to known classical algorithms. In recent years a number of efforts based on continuum methods using QLSA [17, 18], variational quantum algorithms [19, 20], amplitude estimation methods [21, 22], and quantum-inspired methods [23], have been undertaken to solve linear and nonlinear PDEs. However most of these efforts have been theoretical, lacking gate-level quantum numerical simulations and analysis of the resulting flow field, or proper estimates of the actual errors involved.

In particular, a full-gate level quantum simulation is implemented on QFlowS to solve the unsteady Poiseuille and Couette flow problems, extendable with little change to the advection diffusion problem with constant advection velocity. We implement both the fundamental form of QLSA, called the Harrow-Hassidim-Lloyd (HHL) algorithm [24] and its more recent counterpart, [25] based on the linear combination of unitaries (LCU). In addition, we prescribe suitable quantum state preparation protocols and propose a novel quantum post-processing (QPP) protocol to compute *in situ* nonlinear functions of the resulting flow solution. In particular we obtain the viscous dissipation rate $\varepsilon = \nu \langle (\frac{\partial u}{\partial y})^2 \rangle$ of the flow field u and viscosity ν . Together, this forms an end-to-end implementation, which alleviates, to some extent, the caveats of both quantum state preparation and the measurement of qubits—which are otherwise the major limiters of the theoretical quantum advantage [11, 17, 24, 26]. Although the proposed algorithms are far from realistic fluid simulations, they make quantum implementations more amenable for small systems, and inform the running of codes on near-term NISQ machines while attempting to preserve the quantum advantage.

LINEAR FLOW PROBLEMS

We consider the well known 1D unsteady Poiseuille and Couette flows (schematic shown in *SI Appendix* figure S1(a) that are linear dissipative flows which describe for instance, micro-channel flows (e.g., in micro-chips, blood capillaries and syringes) or lubricant flows around bearings. The framework outlined in this work is readily extendable to the linear advection-diffusion eq. (2) with constant advection velocity. More generally, this algorithm caters to the class of elliptic and parabolic PDEs described by d-dim Laplace, Poisson and heat equations. Under certain boundary conditions, the flows under discussion admit exact analytical solutions, thus making them ideal candidates for evaluating the performance of the quantum solver. Some earlier works such as [27, 28] made some important observations in possible implementations on QC for similar problems and estimated theo-

retical upper bounds of their complexities. The general form of the governing PDEs considered here (assuming no body forces or source terms) are given by the momentum conservation and continuity relations of the kind

$$\frac{\partial \mathbf{u}}{\partial t} + \mathbf{C} \cdot \nabla \mathbf{u} = \frac{1}{Re} \nabla^2 \mathbf{u} - \nabla \mathbf{p}, \quad (1)$$

$$\frac{\partial \mathbf{u}}{\partial t} = \frac{1}{Re} \nabla^2 \mathbf{u} - \nabla \mathbf{p}, \quad (2)$$

$$\nabla \cdot \mathbf{u} = 0. \quad (3)$$

where $\mathbf{u} = (u, v, w)$ is the velocity field, \mathbf{C} is a constant advection velocity, \mathbf{p} is pressure field, $Re = UD/\nu$ is the Reynolds number, U is the characteristic velocity, ν is the kinematic viscosity and D is the separation between the boundaries. Eq. (3) enforces the incompressibility condition while eq. (2) describes the well-known unsteady channel (or Poiseuille/Couette flow) (with $\mathbf{C} = 0$ in eq. (1)) which in the 1D case (running example for all discussions from here on) reduces to

$$\frac{\partial u}{\partial t} = \frac{1}{Re} \frac{\partial^2 u}{\partial y^2} - \frac{\partial p}{\partial x}, \quad (4)$$

where the velocity varies only along y (wall-normal direction), and the pressure gradient $\frac{\partial p}{\partial x}$ is set to be a constant. The boundary conditions are no-slip with $u(0, t) = u(D, t) = 0$ for the Poiseuille flow and $u(0, t) = 0$ and $u(D, t) = 1$ for the Couette flow. The initial condition for the temporal evolution is set to be a uniform flow $u(y, 0) = u_{in} = 1$.

We reiterate that this problem is simple from the standpoint of the sophisticated advances of classical CFD. However, this is an excellent starting point for demonstrating the viability of quantum algorithms for CFD, which is the spirit in which this work is presented.

Hybrid quantum-classical numerical setup

The goal now is to solve eq. (4) by means of QLSA, which thus necessitates eq. (4) to be recast as a linear system of equations. To do this, we consider the method of finite differences to discretize the computational domain in both space and time. Details of these schemes, their stability considerations and the resulting matrix equations that form the input to the quantum algorithm is outlined in *SI Appendix*, Section 1.A. The well-known second order central difference scheme is used to discretize the Laplacian operator for N_g grid points, while both forward and backward Euler (FE and BE from here on) schemes are implemented to discretize time, which yield the set of three possible matrix equations $\mathbf{A}_{be1}\bar{u} = \mathbf{b}_{be1}$, $\mathbf{A}_{be2}\bar{u} = \mathbf{b}_{be2}$ and $\mathbf{A}_{fe}\tilde{u} = \mathbf{b}_{fe}$.

To solve these equations, a hybrid quantum-classical method is developed (schematic flow chart is shown in figure 1(b)). The preconditioning and computations of

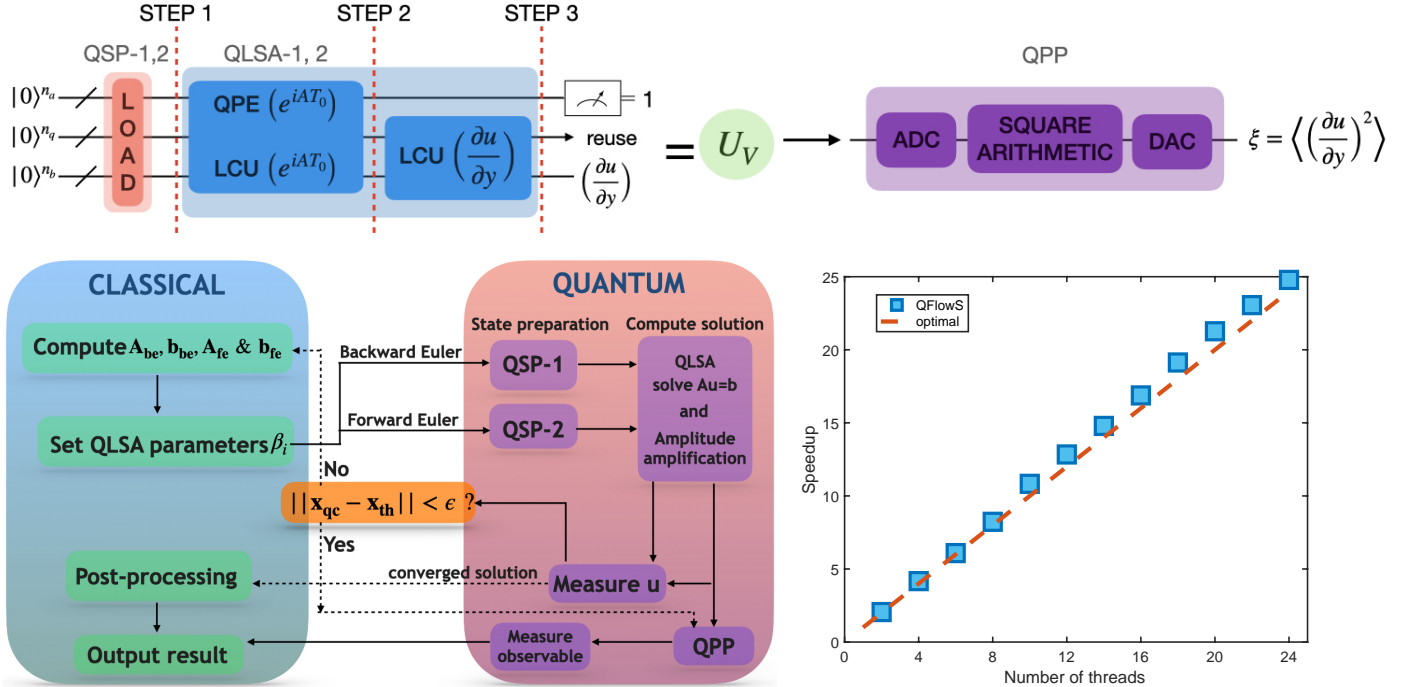


FIG. 1: (a) shows the modified QLSA circuit with QSP, forming an oracle U_V that is employed recursively in the QPP protocol for computing viscous dissipation rate by a combination of Quantum Analog-Digital converters. (b) The working flowchart of the hybrid quantum-classical algorithm. (c) The strong scaling performance of QFlowS with super-linear speedup when run on single node, parallelized with OpenMP up to a total of 24 threads on NYU’s Greene supercomputer. The performance is for simulations of a 20 qubit circuit of depth 422, performing a Quantum Fourier Transform (QFT) and inverse QFT algorithm. The standard deviations are smaller than the blue square symbols around the mean, computed over an ensemble of 8000 simulations with random initial quantum states.

the elements of the matrices \mathbf{A}_{be1} , \mathbf{A}_{be2} , \mathbf{A}_{fe} and vectors \mathbf{b}_{be1} , \mathbf{b}_{be2} , \mathbf{b}_{fe} are done classically. Certain parameters required (as elucidated later) for quantum state preparation (e.g., rotation angles and decision trees) and for Hamiltonian simulation (time T_0^*) are pre-computed classically as well. N from here on refers to the dimension of final matrix system that results from these considerations. With this on hand, the inputs are first loaded on the QC by the quantum state preparation algorithms (QSP-1,2) and the resulting linear system of equations is then solved by QLSA. In the case of iterative BE, $\mathbf{A}_{be1}\bar{u} = \mathbf{b}_{be1}$ is solved for velocities \bar{u} , at every time step until convergence (residue reaching a tolerance $\leq \epsilon_{tol} = 10^{-6}$), which is checked classically. In a contrasting setup, BE and FE are used to set up, respectively, $\mathbf{A}_{be2}\tilde{u} = \mathbf{b}_{be2}$ and $\mathbf{A}_{fe}\tilde{u} = \mathbf{b}_{fe}$, giving $\tilde{u} = [u(y, 0), u(y, dt), \dots, u(y, T)]$, in one shot, $\forall t \in [0, T]$. It is important to note that even the BE method can be setup such that the solution is computed $\forall t$ in one go. However, in the absence of efficient state preparation and measurement protocols, measuring the solution and re-preparing the state for the next time step are $\mathcal{O}(N_g)$ operations that eliminate any quantum advantage, making the overall algorithm no better than clas-

sical solvers (and with additional errors due to quantum measurements). In any case, it is still worthwhile establishing how the method fares as a plausible alternative to classical simulations.

The final solution is either: (a) simply read by quantum measurements for post-processing on a classical device, or (b) the solution is post-processed using the QPP protocol introduced here *in situ* for a quantum device. The former, at the level of a simulator, allows one to validate the correctness of solutions and redesign the circuit as required. While in the latter case, only a single target qubit and few ancillas are measured, which outputs *one* observable—which is a real-valued *nonlinear* function of the velocity field. Apart from computing nonlinear functions, this circumvents expensive and noisy measurements of entire quantum states and more importantly preserves quantum advantage (to the extent possible).

QUANTUM FLOW SIMULATOR - QFLOWS

In [12, 29] several commercially available quantum simulation packages are listed. Most of them, for instance Qiskit (IBM), Quipper [30] and QuEST [31], are

constructed for general purpose quantum simulations and are highly optimized for such operations, making it hard to customize the fundamental subroutines and data structures for CFD calculations. On the other hand, there are softwares such as ANSYS and OpenFOAM that perform solely classical CFD simulations. With the motivation of having a single bespoke quantum simulator for CFD, we unveil here a high performance, gate level quantum-simulation toolkit, which we call *QFlowS*; it is based on a C++ core and designed to be used both independently or as part of other software packages. It has a current capability of 30+ qubit simulation of custom quantum circuits. It also has several built-in gates and quantum circuits that could be used readily, while also being able to probe different quantum state metrics (such as the norm, density matrix and entanglement). Along with these, it includes basic CFD tools needed to set up flow problems making it versatile for QCDFD simulations. Noise modelling is in progress and forms the major part of future software development. *QFlowS* is also continually being parallelized for optimal performance on supercomputers. For instance, figure 1(c) shows the strong scaling performance using OpenMP. The performance is measured while running on NYU’s Greene supercomputing facility. On a single medium-memory computer node (48 cores: 2x Intel Xeon Platinum 8268 24C 205W 2.9GHz Processor) and for a choice of 20 qubits, we measure the run-time (by omitting the one-time initial overhead processes) of a QFT-IQFT circuit action on an ensemble of randomly initialized quantum states. We observe near optimal and at times super-optimal scaling with increasing number of threads up to 24. (Super-optimality arises when the quantum circuit is sparse, causing lesser quantum entanglement. Every single circuit layer operation is distributed over many worker threads, whose cache size exceeds the size of quantum state subspace being handled, thus making them closely parallel). *SI Appendix*, Section 2, summarizes features of *QFlowS*.

QUANTUM LINEAR SYSTEMS ALGORITHM (QLSA)

One of the first quantum protocols for solving equations of the form $A\vec{x} = \vec{b}$ is the HHL algorithm [24] which we refer to here as **QLSA-1**. In [24] it was shown that: *For a hermitian and non-singular matrix $A \in \mathbb{C}^{2^n \times 2^n}$, vector $b \in \mathbb{C}^{2^n}$ ($N = 2^n$), given oracles to prepare A and b in $\mathcal{O}(\text{polylog}(N))$, and a prescribed precision of $\epsilon > 0$, there exists an algorithm that computes a solution x such that $\| |x\rangle - |A^{-1}b\rangle \| \leq \epsilon$ in $\mathcal{O}(\text{polylog}(N)s^2\kappa^2/\epsilon)$* , where κ is the condition number of the matrix. This shows that the algorithm is exponentially faster than classical alternatives, but there are important caveats [26]). Later works [32, 33] attempted to address these caveats, while some others [34–36] fundamentally improved the method by reducing error complexity from $\text{poly}(1/\epsilon)$ to $\text{poly}(\log(1/\epsilon))$. Consequently refs. [17, 35, 37] led to a

more precise class of QLSA methods based on the linear combination of unitaries (LCU) [25] which we shall refer to as **QLSA-2**. In [25] it was shown that under similar caveats of QLSA-1, we have: *For a hermitian and invertible matrix $A \in \mathbb{C}^{2^n \times 2^n}$, vector $b \in \mathbb{C}^{2^n}$, given oracles to prepare A and b in $\mathcal{O}(\text{polylog}(N))$, and a prescribed precision of $\epsilon > 0$, there exists an algorithm that computes a solution x such that $\| |x\rangle - |A^{-1}b\rangle \| \leq \epsilon$ in $\mathcal{O}(\text{polylog}(N/\epsilon)\kappa)$* . This work implements algorithms due to both these methods [24, 25]. In the QCDFD context, we now explore methods suitable for preparing $\{\mathbf{b}_{be1}, \mathbf{b}_{be2}, \mathbf{b}_{fe}\}$ and the matrices $\{\mathbf{A}_{be1}, \mathbf{A}_{be2}, \mathbf{A}_{fe}\}$, to enable the post-processing of the solution \tilde{u} , in order to construct an end-to-end method.

Quantum State Preparation

To prepare quantum states that encode \mathbf{b}_{be1} , \mathbf{b}_{be2} and \mathbf{b}_{fe} , we implement two different methods, both offering sub-exponential circuit depth complexity:

(1) In the case of iterative BE, the vector \mathbf{b}_{be1} , prepared at every time step, is generally fully dense with sparsity $s_b \sim \mathcal{O}(N_{be1})$. In the specific cases of Poiseuille and Couette flows, and for the specific initial conditions considered here, the state prepared at every time step forms a discrete log-concave distribution (i.e., $\frac{\partial^2 \log(b)}{\partial y^2} < 0$ for $\forall t \geq 0$), which could also be confirmed from the analytical solution given by eq. (5) known for this case as

$$u(y, t) = \sum_{k=1}^{\infty} \left[\frac{2(1 - (-1)^k)}{k\pi} \left(1 + \frac{\partial p}{\partial x} \frac{Re}{(k\pi)^2} \right) \sin \left(\frac{k\pi y}{D} \right) e^{\frac{-t}{Re} \left(\frac{k\pi y}{D} \right)^2} \right] - \frac{Re}{2} \frac{\partial p}{\partial x} y(1 - y). \quad (5)$$

Even if the exact solution is not known, provided the initial condition is the only state preparation involved in the algorithm, flexibility exists for most flow simulations in choosing initial conditions that are log-concave, so that one could invoke a *Grover-Rudolph* state preparation [38] technique (or its more evolved off-springs [39, 40]) to offer an efficient way to encode data. Two comments are useful. (i) Though this method could be used for arbitrary state-vectors (at the cost of exponential circuit depth), for an efficient state preparation, some information on the functional form of the state needs to be known *a priori*—from analytical solutions, classical CFD, or by the measurement of the quantum circuit at intermittent time-steps, peeking into its instantaneous functional form. Here, we implement a similar method, which we shall refer to as **QSP-1**, based on [38, 41], where it was shown that: *Given a vector $\mathbf{b}_{be1} \in \mathbb{R}^{N_{be1}}$, state \mathbf{b}'_{be1} can be prepared such that, $\| |\mathbf{b}_{be1}\rangle - |\mathbf{b}'_{be1}\rangle \| < \mathcal{O}(1/\text{poly}(N_{be1}))$ in $\mathcal{O}(\log(N_{be1}))$ steps.* (ii) Measuring all qubits of the register ($\sim \mathcal{O}(N_{be1})$) at every time step compromises

the exponential speed-up and could introduce measurement errors. However, such a method of recursive state preparation and measurement could still prove to be useful with quantum advantage for a very small number of qubits [42]. In any case, we implement this method here to explore if such a BE scheme gives accurate results with or without quantum advantage.

(2) In the case of the one shot methods, an alternative quantum state preparation method can be considered since \mathbf{b}_{fe} is generally larger in size $\sim \mathcal{O}((m+p)N_g)$ (this discussion applies similarly to \mathbf{b}_{be2}). When considered together with all other registers that are initially set to $|0\rangle$, \mathbf{b}_{fe} is a highly sparse state vector with $s_b \sim \mathcal{O}(N_g m)$. For such states, we implement a sparse state preparation protocol [43], which we shall refer to as **QSP-2**. It provides an optimal circuit depth that scales only polynomially with vector size. This method involves constructing decision trees forming an alternative way to represent quantum states. Careful optimization on the structure of these trees leads to efficient state preparation whose complexity depends on the number of continuous pathways in the resulting tree structure. Thus, rephrasing here the result in [43], we have: Given an n -qubit initial state of size $N = 2^n$, all set to $|0\rangle$, except for a sparse vector subspace $\mathbf{b}_{fe} \in \mathbb{R}^{N_{fe}}$ ($N_{fe} = \mathcal{O}((m+p)N_g)$), with sparsity $s_b = m \ll N$, then with only single qubit and CNOT gates, one can prepare such a state with in $\mathcal{O}(2kn)$ time, $k \times \mathcal{O}(n)$ CNOT gates and using 1 ancillary qubit, where $k(\leq m)$ is the number of branch paths of the decision tree.

Both QSP-1 & 2 are elucidated with an example in *SI Appendix*, Section 3.

FLOW SIMULATION RESULTS

We construct and solve the system given by eqs. (4) for $N_g = 10$ and $Re = 10$. We observe that the quantum solutions for the velocity field capture the physics both qualitatively and quantitatively. To discuss closely the utility of QFlowS we consider results from QLSA-1. As shown in figure 2(a) the converged steady state solution (using iterative BE) undershoots the analytic solution for 7 qubits, and performs better with a higher number of qubits ($Q_{PE} \geq 14$) that are allocated for the Quantum Phase Estimation (QPE) algorithm, which in turn decides the quantum numerical precision. Similarly, the converged solution for the one shot FE and BE cases also become more accurate with respect to both analytical and classical CFD solutions, with increasing number of qubits, as seen in figure 2(c) and (d) respectively.

Our experience is that, between the three schemes, the one shot FE and BE turns out to be more accurate than iterative BE for increasing number of qubits, as shown in figure 3(a), where the error ϵ_{rms} is computed with respect to the analytical solution. Among the two, one shot schemes, though quantitatively their error behavior

is nearly the same, (i) We see some spurious oscillation like error in the velocity profile for the BE case as seen in figure 2(d) for higher Q_{PE} . (ii) The BE case however has no stability based restrictions as the FE case making it more flexible on the choice of dt . (iii) When accuracy in temporal discretization is of the concern the one shot FE fares better. The performance can also be measured by computing the fidelity of the solution as shown in the inset of figure 3(a), which shows the BE to perform better than FE. However fidelity might not always be a good indicator to performance as illustrated in *SI Appendix* Section 1.B. Both QLSA-1 and QLSA-2 rely on a variant of the phase estimation algorithm which generally contributes most to the total error QPE; in QLSA-2, the Gapped Phase Estimation (GPE) is rather computationally inexpensive and less erroneous than in QLSA-1[17]). In the case of phase estimation, the operator/matrix under consideration is exponentiated first as e^{iAT_0} , where T_0 is the Hamiltonian simulation time. An optimal choice T_0^* (unknown a priori) scales on the eigenvalues λ_j that are spectrally decomposed in the basis of A as $\sum_j e^{i\lambda_j T_0^*} |u_j\rangle\langle u_j|$ to produce the best Q_{QPE} -bit binary representation $|\tilde{\lambda}_j\rangle_{Q_{QPE}}$. It also minimizes possible truncation errors and any spurious quantum numerical diffusion.

In case of QLSA-1 it is important to note, since we are interested in estimating λ^{-1} eventually, the smallest eigenvalue will contribute the most to the error. Therefore ensuring that the smallest value representable (least count) with Q_{PE} qubits $= 2^{-Q_{PE}}$ is $\leq \tilde{\lambda}_{min}$ is essential. The error for all cases shown in figure 3(a) has a gradual step like decay because increasing Q_{PE} in small steps (of $\mathcal{O}(1)$) does not lower the least count appreciably (in \log_{10} or \log_e) as Q_{PE} gets larger. In case of QLSA-2, though it evades a full blown QPE, the right choice of T_0 (for the Fourier approach [17]) and the LCU coefficients is still crucial for better accuracy.

At the level of the flow field when we probed further, the choice of T_0 seemed to exhibit non-trivial effects; for instance, in the iterative BE case, when gradually increasing Q_{PE} qubits, the converged solution either undershot or overshot the analytical solution initially. This is captured in figure 3(b), where the error ϵ (with respect to the analytical solution \mathbf{u}_{an} of the center line velocity solution) oscillates around $\epsilon = 0$ before converging to it for $Q_{PE} > 12$. For the specific case shown here, a choice of $T_0^* = 1.75$ (dotted black line) has the least oscillation of the error and best accuracy.

We can now ask: what combination $TQ = (T_0, Q_{PE})$ gives the least error? To answer this better, we take a sample matrix equation system (of size 8×8 and $\kappa = 18.8795$) and solve it for different TQ . We then make a contour plot of the QLSA error $\epsilon_{QLSA} = \|u_Q - u_C\|$, as shown in figure 3(c) and trace the path of least error ϵ_{min} for each TQ . Further, the range of the T_0 scan can be reduced with some initial estimates to the lower and upper bounds of λ_{min} and λ_{max} [44] such as, $\beta_1 - \beta_2 \sqrt{N-1} \leq \lambda_{min} \leq \beta_1 - \beta_2 / \sqrt{N-1}$ and

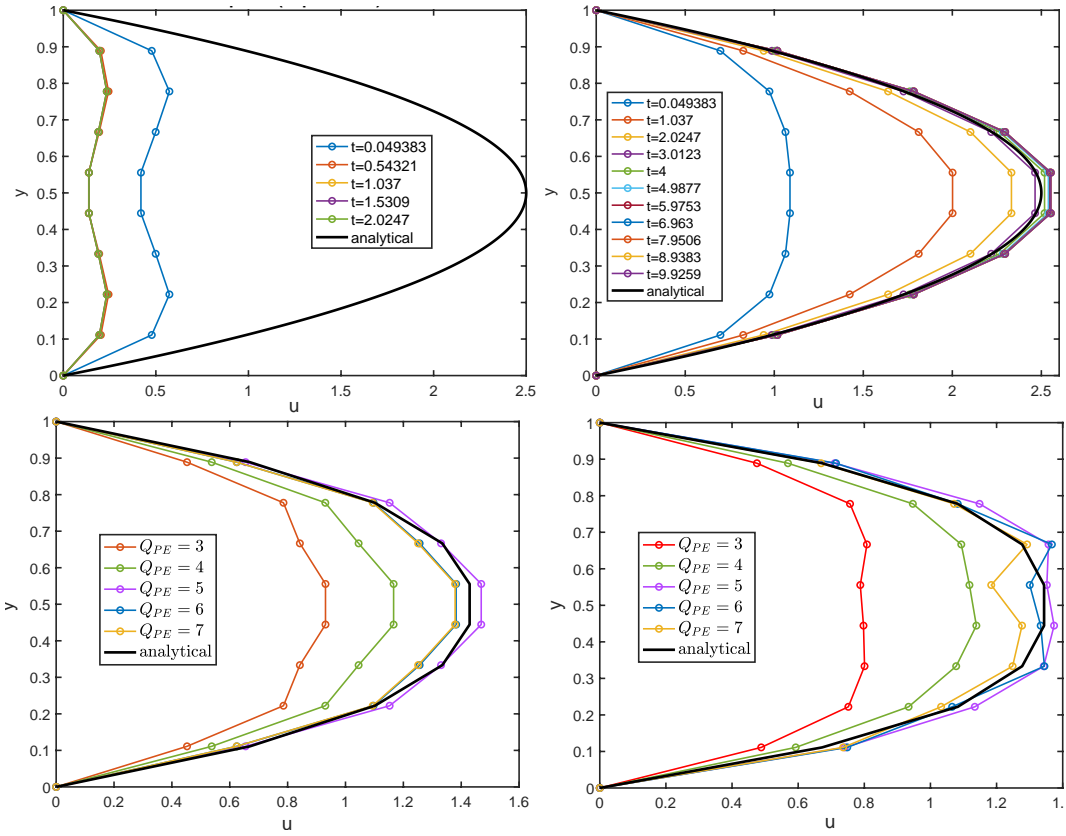


FIG. 2: (a) and (b) show the quantum simulation of the flow field evolving forward in time towards steady state (analytical parabolic solution shown as solid black line) using BE scheme that uses 7 and 14 qubits (3 and 10 QPE qubits (Q_{PE}), respectively), for $N = 10$, $Re = 10$, $\partial p / \partial x = -2$ and $dt = 0.01$. The accuracy of the converged solution improves for higher Q_{PE} . Here the velocity field is solved for at every time step; (c) shows increasingly accurate converged solutions with increasing $Q_{PE} \in \{3, 4, 5, 6, 7\}$, but solved using the FE scheme where the velocity field is solved for all time steps in one shot, and only the final solution is extracted. Here $\alpha = 0.5$ is set to meet the the von Neumann stability criterion and the parameter $T_0^* = 5.0$ is fixed. (d) also shows the one shot method, solved with a BE scheme. Though $\alpha = 0.5$ is set to maintain the same time step size as (c) for comparison), there is no hard constraint given that the method is unconditionally stable. Here $T_0^* = 8.5$.

$\beta_1 + \beta_2 / \sqrt{N-1} \leq \lambda_{max} \leq \beta_1 + \beta_2 \sqrt{N-1}$, where $\beta_1 = \text{Tr}(A)/N$ and $\beta_2 = (\text{Tr}(A^2)/N - \beta_1^2)^{1/2}$. We observe that the optimal T_0^* for all combinations lies in a fairly small range $\Delta T_0 \sim 0.1$. This is a unique value lying along the median of this range, $T_0^* \approx 1.3$ for which the system performs best. This means that all or most eigenvalues are best represented in binary form with Q_{QPE} qubits (one or some of the eigenvalues could also turn out to be represented exactly). Further, given T_0^* , with increasing number of qubits, the minimum error exhibits a power law decay $\epsilon_{min} \sim Q_{PE}^{-6.81}$ as shown in figure 3(d), reaching $\sim 10^{-5}$ at around 13 qubits. The exponent becomes increasingly negative with decreasing κ , since the range of eigenvalues becomes smaller and more eigenvalues tend to be easily representable with a given number of qubits. The thick horizontal red line shows the least count for $Q_{PE} = 13$; here, $\epsilon_{min} < 2^{-13}$. This favorable possibility arises because a subspace of the solution set could have had near exact representation using the given number of

qubits, which lowers the overall L2 error $\leq 2^{-Q_{PE}}$. This means the minimum number of qubits needed to attain an error ϵ grows as a power law $(Q_{PE})_{min} \sim 2.92\epsilon^{-0.1158}$, as shown in the inset of figure 3(d). If not for the right choice of T_0^* , for $Q_{PE} > 3$, one would spend more numerous qubits $\mathcal{O}(1.44 \log(\epsilon^{-1}))$ to lower the overall error. We note that ϵ as computed here suppresses the error from finite differences, which is $\epsilon_{fd} \sim \mathcal{O}(\Delta y^2, \Delta t)$ and it's important to note that this error plagues both quantum and classical solutions. The quantum solution, however, gets closer to the classical solution with increasing qubits ($Q_{PE} = 9$, yellow curve).

Thus, being able to estimate T_0^* fairly accurately reduces the overall computational resources required as well as the error, making it amenable for NISQ devices. Though there have been several analytical, asymptotic prescriptions for the choice of T_0^* [17, 24, 45], the exact choice remains elusive. To shed better light, QFlowS is equipped with QPE optimizer subroutine which, on

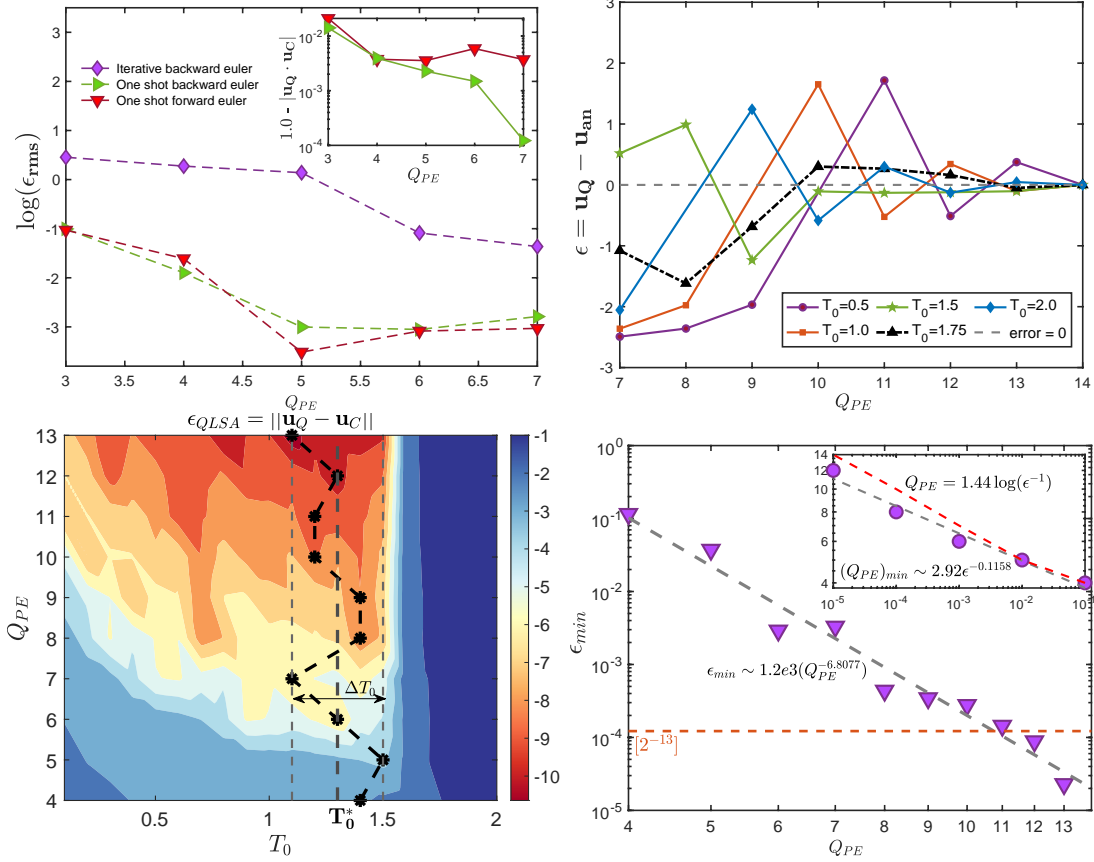


FIG. 3: (a) shows the value of absolute root-mean-square (RMS) error for the BE and FE cases shown in 2((a)-(c)) against QPE qubits of both the step-by-step and one shot methods. To compare directly the one shot BE and FE methods, we show in the inset the quantity (1-fidelity) as a function of Q_{PE} . (b) shows the absolute error computed with respect to the analytical solution for varying T_0 . The black dotted line joining upright triangles shows the case for which the error magnitude and oscillation around the zero line are the least. (c) shows the contour plot of the QLSA root-mean-square error ϵ_{QLSA} computed with respect to the classical inversion solution for different $TQ = (Q_{\text{PE}}, T_0)$ pairs. The dotted black line traces the locus of the least/minimum error for each (T, Q) pair in that range, which shows an oscillation around a unique median value T_0^* specific to a given matrix (or κ). (d) shows the decay in the $(\epsilon_{\text{QLSA}})_{\text{min}}$, extracted from (c) with respect to only Q_{PE} for a fixed $\kappa = 18.8795$ and $T_0^* = 1.3$. The inset plots the Q_{PE} (ordinate) required to achieve a specified ϵ_{QLSA} (abscissa).

the basis of the nature of the flow problem and the numerical method (finite differences) used, estimates T_0^* by very minimal classical pre-processing. Since κ decides the range of eigenvalues and the invertibility of the matrix, it forms a common link that characterizes matrices for different systems with similar sparsity. Therefore, a relation that uniquely connects κ with T_0^* would make a reasonable basis for prescribing T_0^* for different system configurations. We provide such a relation which, though generalizable in behavior, is specific to: (1) the class of elliptic and parabolic linear PDEs considered here; (2) finite difference based numerical formulations that give rise to either sparse, band diagonal, lower triangular, Toeplitz or circulant matrices.

Since the one shot FE and BE seems to perform better than BE, we take the matrix system of the former for $N_g = 10$ and characterize how κ varies as a function of

matrix size $m = \lceil \log_2(T/dt) \rceil$ and viscosity $\nu = 1/Re$. Figure 4(a) shows for a specific case of $T = 1$, $dt = 0.001$, κ grows as a stretched exponential with decreasing (increasing) ν (Re) and saturates for very low ν , while for a fixed $\nu = 0.1$, κ grows exponentially with m as shown in the inset of figure 4(a). However, the overall behavior of κ with both ν and the system size m is shown in figure 4(b), where the $\kappa - \nu$ curves transition from exponential to stretched exponential fits as plotted for increasing m obtaining the relation $\kappa \leq m(e^{-0.02m\nu} + 2)$. This relation confirms that κ is bounded and is not exponentially large. Here we explicitly highlight the dependence of κ on ν and note that it is also bounded from above by $\kappa = 3(m + p + 1)$, as given in [13] for nonlinear PDE systems that generally have higher κ than linear PDE problems. In both cases, κ increases with Re and m .

With this relation in hand, we proceed to compute

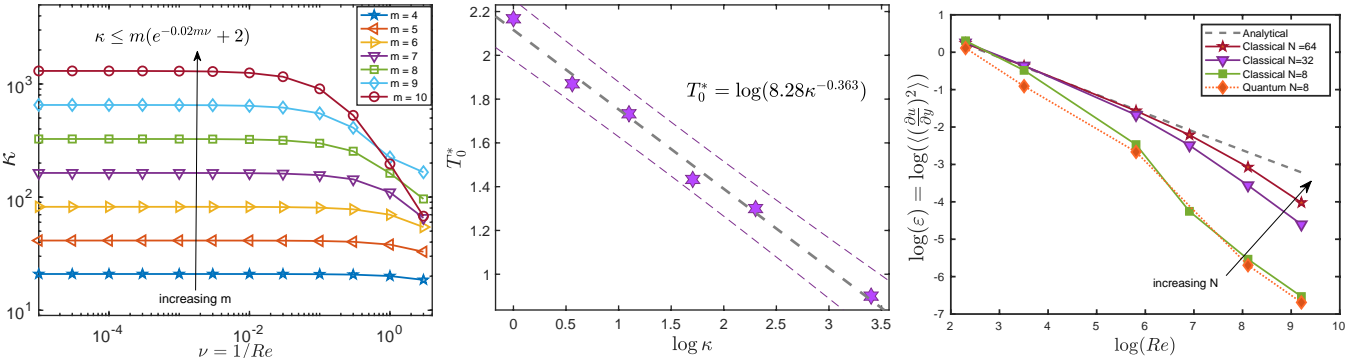


FIG. 4: (a) shows the behavior of κ with increasing m and decreasing ν . For $\nu < 0.01$, κ saturates to a constant that is decided largely by m . This is expected since for Poiseuille flow, by appropriately scaling time with ν (using $t^* = \nu t / L^2$), ν can be absorbed into the equation. However, this is not the case when $\mathbf{C} \neq 0$ in eq. 1, in which case ν would have a much stronger effect on κ . (b) Using QFlowS, a small sample space of low dimensional matrices for varying κ is solved to compute T_0^* in each case, as shown in figure 2(c), which yields a power law scaling of T_0^* against κ , as marked in the figure. This feature can be used to predict T_0^* for higher dimensional matrices. T_0^* is insensitive to κ below a threshold value of ν for these problems. Thin dashed lines indicate 99% levels. (c) shows the mean viscous dissipation rate ε with respect to increasing Re (decreasing ν) computed from quantum solutions.

T_0^* for increasing κ , by extracting, as before, the TQ phase diagram and finally obtaining the relation $T_0^* \sim -0.363 \log(\kappa) + 0.918$. In practice, only a small zone of the phase diagram is explored. The effect of ν is as one would expect, with T_0^* decreasing and saturating for very low values. Now this relation between $T_0^* - \kappa$ obtained via simulations on QFlowS serves as an ideal source for choosing T_0^* appropriately to perform accurate simulations for bigger circuit sizes as well. The earlier relation (despite a slight variation with matrix structure) forms a reasonable approximation for T_0^* for all systems considered here. This process predicts optimal T_0^* for Hamiltonian simulation algorithms for both QLSA-1 and QLSA-2. In case of QLSA-2, QFlowS also efficiently generates the set of the LCU coefficients for optimal performance. Further, even for other class of problems (different PDEs and discretization schemes), QFlowS's QPE optimizer could be employed to perform similar low cost classical pre-processing to suggest optimal T_0^* for accurate and efficient fluid flow simulations. Further, barring minor quantitative differences, on performing a similar analysis on the Couette flow case we find that the qualitative outcome and inferences drawn are nearly the same as that of the Poiseuille flow case as seen here. The corresponding velocity profiles for the Couette flow are shown in *SI Appendix* Section 1.B.

QUANTUM POST-PROCESSING PROTOCOL (QPP)

Once the velocity field is obtained, measuring it by repeated execution (excluding the requirements of quantum amplitude amplification [46]) of the quantum circuit ($\mathcal{O}(N)$ complexity) will compromise any quantum ad-

vantage and also introduce measurement errors. Here, we examine a QPP that produces just one real-valued output of the average viscous dissipation rate per unit volume, $\varepsilon = \nu \langle (\partial u / \partial y)^2 \rangle$ (by requiring only a very few measurements). Given that we are equipped with an oracle U_V (QLSA-2) that prepares a quantum register with the velocity field solution, we append to it a derivative module that computes first $\frac{\partial u}{\partial y}$ of the solution depicted in the circuit diagram shown in figure 1(a). This is done by either (1) the LCU method where a finite difference matrix of first derivative is decomposed as linear combination of unitaries, or (2) a spectral method in which an IQFT is first applied to enter the conjugate space and the first derivative is now a simple scalar multiplication with the corresponding wavenumber, k . Finally the application of QFT transforms it back into real space.

At this point, if one is interested in general nonlinear functions such as trigonometric, logarithmic, square-root or higher powers, we implement the following procedure. The derivatives that are stored as quantum amplitudes are first converted into an n_m -bit binary representation using Quantum Analog-Digital Converter (QADC) [47]. Following this step, a direct squaring algorithm outlined in *SI Appendix* Section 4, or a binary quantum arithmetic squaring circuit (an inverse of the square-root algorithm, which is more expensive than the former, see [48]) is used to compute $(\frac{\partial u}{\partial y})^2$, which are finally converted back into amplitude encoding using Quantum Digital-Analog Converter (QDAC) [47]. This algorithm requires $\mathcal{O}(1/\epsilon_{QPP})$ calls to the controlled- U_V oracles (that has a complexity of $\mathcal{O}(\text{polylog}(N/\epsilon)\kappa)$, thus an overall complexity of $\mathcal{O}(\text{polylog}(N/\epsilon)\kappa/\epsilon_{QPP})$), one query to the bit-squaring algorithm with complexity $\mathcal{O}((\log_2 N)^2)$ and $\mathcal{O}((\log_2 N)^2/\epsilon_{QPP})$ single- and two-qubit gates. The outline of the QPP algorithm introduced here along with

circuit implementation is given in circuit *SI Appendix* Section 4.

As a final step we apply a matrix U_{avg} that computes the sum of derivatives at all points into one qubit, measuring which, along with a few ancillas, outputs the desired ε (after some normalization and multiplication by ν). Applying QPP on the quantum solution yields a behavior of ε with Re , computed at $T=0.2$, as shown in figure 3(c). Since the initial condition is a uniform flow, in the beginning there will be sharp gradients near the wall. To capture them, one would need a large number of grid points since the error in $\partial u / \partial y$ is $\epsilon \approx \mathcal{O}(\Delta y)$. This effect is seen clearly from figure 3(c), where the classical dissipation computed for $N_g = 8, 16$ and 64 shows improving trends; for high enough N , it begins to closely follow the analytical result. We pick the case of $N_g = 8$ for the quantum case and see that it follows closely the corresponding classical solution for a total of 13 qubits. This could be made more accurate with more of the QPE qubits and the resolution N_g , as seen before. In essence, this demonstrates the possibility for computing quantities such as ε effectively as a quantum post processing step.

DISCUSSION

We have demonstrated here a possible quantum algorithmic strategy and its full implementation using gate-based quantum circuits on QFlowS, to simulate Poiseuille and Couette flows in an end-to-end manner. First, we identify suitable quantum state preparation algorithms by considering the sparsity and functional forms of the initial velocity data being encoded. In CFD, it is generally admissible to choose a relatively simple form and a sparse initial condition, which would result in a relatively low cost of state preparation. QSP-1,2 could both be used as shown here, by assessing the form of input to encode initial and boundary conditions with sub-exponential complexity ($\mathcal{O}(\log(N_{be}))$ and $\mathcal{O}(kn)$, respectively), as well as to re-initialize instantaneous velocity fields. However, data that are dense with no functional form would force an exponential circuit depth.

Second, using finite difference schemes, the governing equations were discretized to form linear system of equations, and solved by implementing QLSA-1 and -2, which are state-of-the-art, high precision algorithms with exponential advantage compared to classical schemes. Here, we have made a detailed analysis of the behavior of the velocity solutions and the attendant errors, which have revealed that FE outperforms BE. Further, we proposed the role of T_0 and discussed algorithms to prescribe the optimal value T_0^* . The power-law and exponential form relations of $(\epsilon_{min} - QPE)$ and $(T_0^* - \kappa)$, respectively, given by QFlowS, forms a well-informed basis to choose T_0^* and minimum required qubits to perform accurate (up to ϵ_{min}) and qubit-efficient fluid flow simulations. Though QLSA-2 evades QPE and can provide exponential ad-

vantage in precision $\mathcal{O}(\text{poly log}(N/\epsilon)\kappa)$, other methods based on adiabatic QC [49] could have potentially simpler implementations, while offering a similar performance, motivating further investigations.

To keep the discussion compact, the data reported here are taken mainly from QLSA-1, but a similarly detailed discussion of simulation results with QLSA-2 forms the bulk of the upcoming work. In QLSA-2 the critical factors computed are the coefficients for LCU, GPE parameters and a comparison between the Fourier and Chebyshev approaches. Further, we have introduced a QPP protocol, where we propose the computation of the viscous dissipation rate ε , using a specific combination of QFT, IQFT, QADC, QDAC and bit-arithmetic, with an overall complexity that scales as $\mathcal{O}(\text{poly log}(N/\epsilon)\kappa/\epsilon_{QPP} + ((\log_2 N)^2/\epsilon_{QPP}))$. The QPP introduces an extra $\mathcal{O}(1/\epsilon_{QPP})$ scaling that brings down the performance of QLSA-2 to the level of QLSA-1 (if $\epsilon \approx \epsilon_{QPP}$). Added to this, for purposes of quantum amplitude amplification, QFlowS is capable of repeating circuit runs in parallel (currently tested up to ~ 8000 shots).

We should point out that this method avoids measuring the entire velocity field, thus protecting it from compromising the quantum advantage and escalating possible measurement errors. We observe that ε computed from the resulting quantum simulations captures the known analytical results. This method can be extended to compute other nonlinear functions of the velocity field.

In summary, along with introducing a new quantum simulator package QFlowS—designed mainly for CFD applications—we also demonstrate a complete implementation of an end-to-end algorithm to perform fluid flow simulations using QC, which paves the way for future QCDFD simulations of both linear and nonlinear flows. However, it is important to note that we have not addressed other key challenges such as noise and quantum error correction, which we emphasize are critical to simulations on near term quantum devices. Also, the complexities of the algorithms provided here are estimates; along with investigating higher order finite difference schemes, a detailed error and complexity analysis along with computing exact gate counts and circuit depths form an important part of ongoing efforts. Extending these methods and tools presented to nonlinear systems such as Burgers equations and Navier-Stokes equations also part of the ongoing efforts.

Data availability

All study data are included in the main text. The package QFlowS will shortly be made available as an open-source package on GitHub.

ACKNOWLEDGMENTS

We wish to thank Dhawal Buaria (NYU), Yigit Subaşı (LANL), Jörg Schumacher (TU Ilmenau), Balu Nadiga (LANL), Patrick Rebentrost (CQT), Stefan Wörner (IBM) and Philipp Pfeffer (TU Ilmenau) for insightful discussions. S.S.B acknowledges the computational resources provided by the NYU Greene supercomputing facility on which these simulations were performed.

Appendix A: Numerical method

1. Finite difference

a. Spatial discretization

The well known 2nd order central difference scheme is used to discretize the flow domain into N_g equidistant grid points, as shown in figure S1(a) ($u = [u_1, u_2, \dots, u_{N_g}]$), with grid spacing $\Delta y = h = 1/(N_g + 1)$, admitting a discretization error $\sim \mathcal{O}(\Delta y^2)$. Since the velocity is known at the boundaries, one solves only for the $N_g - 2$ unknown internal grid points. Thus the Laplacian operator can be written as

$$\Delta u = \frac{u(y_i + h) - 2u(y_i) + u(y_i - h)}{h^2} + \text{h.o.t.} \quad (\text{A1})$$

Now denoting this discretization operator as matrix \mathbf{A} and letting the pressure gradient form a constant vector \mathbf{f} , we can rewrite eq. 2 (in the main text) as

$$\frac{\partial u}{\partial t} = \mathbf{A}u + \mathbf{f}. \quad (\text{A2})$$

b. Temporal discretization:

To integrate in time, the temporal domain $t \in [0, T]$ is discretized into $m = T/\Delta t$ time steps using two different schemes both admitting an error $\sim \mathcal{O}(\Delta t)$:

1. *Backward Euler or Implicit method:* This discretizes the time derivative as

$$\frac{u^{j+1} - u^j}{\Delta t} = \mathbf{A}u^{j+1} + \mathbf{f}, \quad (\text{A3})$$

and gives the matrix equation

$$\mathbf{A}_{be1}\bar{u} = \mathbf{b}_{be1}, \quad (\text{A4})$$

which needs to be inverted recursively to obtain the velocity field at every time step, where $\mathbf{A}_{be1} = -(\mathbf{A}\Delta t - \mathbf{I})$, $\bar{u} = u^{j+1}$ and $\mathbf{b}_{be1} = u^j + \mathbf{f}\Delta t$. This scheme is known to be *unconditionally stable*

with any choice of the size of Δt .

We also set up an alternative matrix equation

$$\mathbf{A}_{be2}\bar{u} = \mathbf{b}_{be2}, \quad (\text{A5})$$

for all time steps as shown in eq. A8. $(\mathbf{A}_{be2})_{ij} = -(\mathbf{I} + A\Delta t) \forall i = j$. However, $\forall i \leq m$, $(\mathbf{A}_{be2})_{ij} = -\mathbf{I}$ for $j = i - 1$ and $\forall i \geq m$, $(\mathbf{A}_{be2})_{ij} = -\mathbf{I}$ for $j = i - 1$. Further, $(\mathbf{b}_{be2})_i = \{u_{in} \forall i = 0; = -\mathbf{f}\Delta t \forall 0 < i \leq m; and = 0 \forall i > m\}$.

2. *Forward Euler or Explicit method:* Here the discretization is given by

$$\frac{u_i^{j+1} - u_i^j}{\Delta t} = \mathbf{A}u_i^j + \mathbf{f}, \quad (\text{A6})$$

which leads to the matrix equation,

$$\mathbf{A}_{fe}\tilde{u} = \mathbf{b}_{fe}, \quad (\text{A7})$$

where \mathbf{A}_{fe} , has a double-banded structure as written in eq. A9, $(\mathbf{A}_{fe})_{ij} = \mathbf{I} \forall i = j$ (see below). However, $\forall i \leq m$, $(\mathbf{A}_{fe})_{ij} = -(\mathbf{I} + A\Delta t)$ for $j = i - 1$ and $\forall i \geq m$, $(\mathbf{A}_{fe})_{ij} = -\mathbf{I}$ for $j = i - 1$. Further, $(\mathbf{b}_{fe})_i = \{u_{in} \forall i = 0; = \mathbf{f}\Delta t \forall 0 < i \leq m; and = 0 \forall i > m\}$.

Equations A8 and A9 thus unroll all the time steps into one big matrix of dimensions $(m+p+1)N_g \times (m+p+1)N_g$, thus solving for the velocity $\tilde{u} = [u^0, u^1, \dots, u^{m+p}]$ at all times in one shot, where every u^j is the full field at all grid points. The total time T is discretized into $m + p$ time steps, where one chooses a large enough p , such that every $u_i^j = u_i^{j+1}$ for $j \in [m+1, m+p]$, which implies that, after the attainment of a steady state, the solution produces p copies of the steady state solution. This is done only to improve the measurement probability of the post-selected state [13] and does not affect the solution itself. This method is stable only for an appropriate choice of Courant number (von Neumann stability criteria), $\alpha = \frac{\Delta t}{(\Delta y)^2} < 0.5$, making it *conditionally stable* and specific to the PDE under discussion, which therefore also decides the upper bound on the largest admissible Δt .

2. Poiseuille flow

The discussion of the Poiseuille flow is provided in the main text and will not be repeated here.

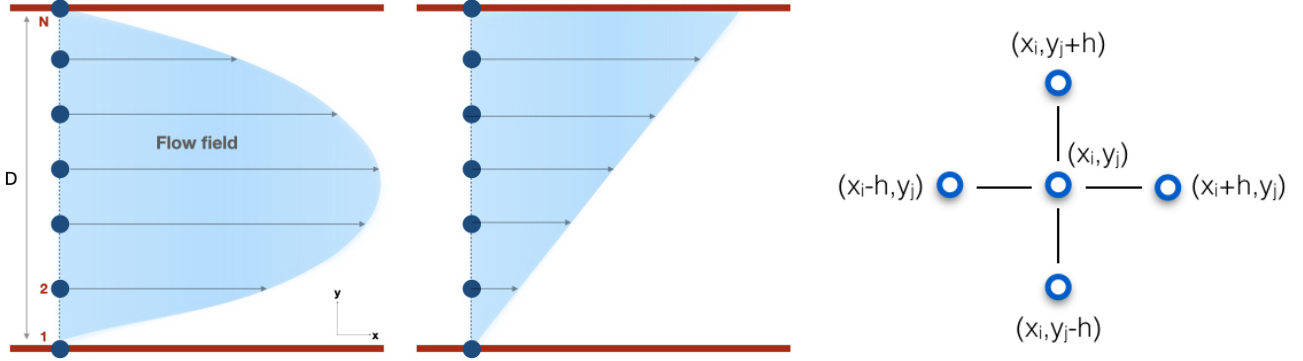


FIG. 5: (a) Shows the computational flow field setup: The flow is confined between two no-slip boundaries separated by a distance $D = 1$, with x and y as the streamwise and wall-normal directions, respectively. The left and right panels in (a) show the schematics of steady state velocity profiles of the Poiseuille and Couette flows, respectively. The finite difference scheme discretizes the flow domain along y into N grid points with separation Δy , at which the velocities are computed. (b) shows the 2nd order central difference stencil in 2D. For the 1D case, only the points in the y -direction are considered and the resulting approximation to the Laplacian operator estimated at a given point y_i using the two points on either side of it is given in eq. A1.

$$\begin{bmatrix} \mathbf{I} & 0 & \cdots \\ -\mathbf{I} & (\mathbf{I} - \mathbf{A}\Delta t) & \\ 0 & \ddots & \ddots \\ \vdots & & -\mathbf{I} & (\mathbf{I} - \mathbf{A}\Delta t) \\ & & & -\mathbf{I} & \mathbf{I} \\ & & & & \ddots & \ddots \\ & & & & & -\mathbf{I} & \mathbf{I} \end{bmatrix} \begin{bmatrix} u^0 \\ u^1 \\ \vdots \\ u^m \\ u^{m+1} \\ \vdots \\ u^{m+p} \end{bmatrix} = \begin{bmatrix} u^{in} \\ b_0 \\ \vdots \\ b_{m-1} \\ 0 \\ \vdots \\ 0 \end{bmatrix} \quad (A8)$$

$$\begin{bmatrix} \mathbf{I} & 0 & \cdots \\ -(\mathbf{I} + \mathbf{A}\Delta t) & \mathbf{I} & \\ 0 & \ddots & \ddots \\ \vdots & & -(\mathbf{I} + \mathbf{A}\Delta t) & \mathbf{I} \\ & & & -\mathbf{I} & \mathbf{I} \\ & & & & \ddots & \ddots \\ & & & & & -\mathbf{I} & \mathbf{I} \end{bmatrix} \begin{bmatrix} u^0 \\ u^1 \\ \vdots \\ u^m \\ u^{m+1} \\ \vdots \\ u^{m+p} \end{bmatrix} = \begin{bmatrix} u^{in} \\ b_0 \\ \vdots \\ b_{m-1} \\ 0 \\ \vdots \\ 0 \end{bmatrix} \quad (A9)$$

3. Couette flow

Following the same procedure as for Poiseuille flow, the Couette flow ($\mathbf{u}(0, t) = 0, \mathbf{u}(1, t) = 1$) can be captured accurately as seen in the flow profiles of figure 6(a-d). Similar inferences as discussed in the main text are applicable in this case as well. We wish to highlight two possible measures of accuracy: (i) the fidelity = $|\mathbf{u}_Q \cdot \mathbf{u}_C|$ and (ii) RMS error (with respect to analytical solution), given by $\epsilon_{rms} = (\langle \mathbf{u}_Q - \mathbf{u}_{an} \rangle)^{1/2}$, which are both plotted in figure 6(e) for a one shot FE scheme with a *nearly* accurate estimate of T_0^* . We can clearly observe that with increasing Q_{PE} , the fidelity increases, though the ϵ_{rms} has a weakly increasing trend. This indicates the that higher

fidelity does not necessarily indicate better ϵ_{rms} , showing that fidelity might not be the most robust measure of performance when solving physical, fluid mechanical problems. Higher fidelity only indicates larger overlap of the quantum solutions with respect to the classical inversion solution, which itself is erroneous due to finite discretization and truncation errors. Even if fidelity=1, the error is still bounded by $\sim \mathcal{O}((\Delta y)^2, \Delta t)$. The solution for the one shot case is a wavefunction that encodes all time steps, but we extract only the final time step. The fidelity is an overall measure of this solution but does not quantify whether the vector subspace corresponding to the final time step is more accurate or not. Also, the fidelity in the iterative BE case drops largely for every

time step, since a dynamical T_0^* is not chosen for every time step. However, higher fidelity can be seen as only an indicator of whether the chosen quantum parameters for QLSA are at least in the reasonable ballpark.

Appendix B: QFlowS - A brief overview of the package

QFlowS is a specialized high performance quantum simulator that enables setting up CFD problems in the QC format seamlessly. We summarize here briefly the various features of QFlowS as schematically depicted in figure 5(a).

1. *Qubits and quantum states:* Qubits which are quantum analogues of classical bits, form the fundamental units of information storage and are represented by quantum states that follow rules of quantum mechanics. Mathematically, they form elements of a complex vector space (Hilbert space $\mathbb{H} (\in \mathbb{C}^n)$). An n-qubit state of the quantum computer, formed by taking tensor products of single qubit states $|\psi\rangle$, is given by

$$|\psi\rangle^{\otimes n} = \sum_{i=1}^{2^n} c_i |u_i\rangle, \quad c_i \in \mathbb{C}, \quad (\text{B1})$$

which encodes 2^n complex values c_i , in the basis $|u_i\rangle$, that are stored as 1-dimensional arrays on QFlowS. The memory required should ideally scale linearly with wavefunction size ($\approx 16 \times 2^n$ bytes with double precision), but there is an overhead due to the need to store quantum circuit instructions. Currently, QFlowS offers simulation capabilities with up to 30+ qubits, which span vector spaces with dimensions of the order $\sim 10^9$. For performing parallelized simulations, these quantum states are either (a) loaded on a *large* memory single node architecture (with or without GPU) dealt with an *OpenMP* style parallelization, or (b) distributed onto different processors for an *MPI* style execution. Both methods were tested initially but the former method was favored because of the simplicity of implementation and lower communication overheads. Some key operations on quantum states that can be done with QFlowS include:

- (a) Quantum State Preparation (QSP) - To initialize any arbitrary states or states with special features. This is detailed further in *SI Appendix*, Section 3;
- (b) Quantum state tomography and amplitude estimation - To estimate the amplitude of the final quantum state by reconstructing the state using different tomography techniques [8];
- (c) Quantum state characteristics - To compute other useful properties of the state such as density matrices, entanglement and norm.

2. *Quantum gates and circuits:* Quantum gates are given by unitary operators U ($UU^\dagger = U^\dagger U = \mathcal{I}$), that are essentially rotation matrices, which collectively form a quantum circuit that manipulates quantum information in a specific way. The quantum circuit can be viewed as a tensor product of all the single qubit gates that forms a matrix of the size $2^n \times 2^n$ for an n-qubit circuit. On QFlowS, the quantum gates are not implemented as matrix operations, but as algebraic operations. The exact transformation caused by different gates is translated into vector operations that affects the specific coefficients, but done in parallel on multiple cores. This makes the simulator more efficient with respect to both memory and speed. For example, a Hadamard gate and a NOT gate acting on a two qubit state shown in figure S4, is given by

The action of such a circuit brings about a transformation on the state, as given by eq. 11. Such a transformation could be algebraically dealt as follows. In an n-qubit circuit, a Hadamard gate acting on the qubit q is H_q , for which $u_i \mapsto \frac{1}{\sqrt{2}}(u_i \pm u_{i+2^{n-q-1}})$. This operation is performed on vector elements by the parallel processing of causally disconnected (unentangled) gates and vector subspaces without having to store or multiply the large $2^n \times 2^n$ matrices. QFlowS can successfully handle circuits with ~ 10 million multi-controlled and two-level gates even on a standard workstation with 10 core CPU, 1TB memory and 32GB RAM.

3. *Algorithm library and portability:* QFlowS is docked with several standard quantum subroutines or algorithms such as Quantum Fourier Transform (QFT) and Quantum Phase Estimation (QPE) that can be readily used in any new circuit. Along with that, QFlowS has classical CFD tools such finite difference (FDM), finite volume (FVM) and boundary element methods (BEM), implicit and explicit time stepping methods, predictor-corrector methods and linearization methods such as Homotopy Analysis Method (HAM) and Carleman method—to highlight a few. These classical subroutines generate appropriate matrices and vectors in formats that can seamlessly be imported by the quantum algorithms. This package will offer easy portability onto both local workstations and supercomputers.

4. *Visualization:* With QFlowS, the quantum states and quantum circuits can also be visualized with an in-built state histogram builder and circuit drawer, with which algorithms and states can be visualized and verified for correctness to simulate and test the circuits.

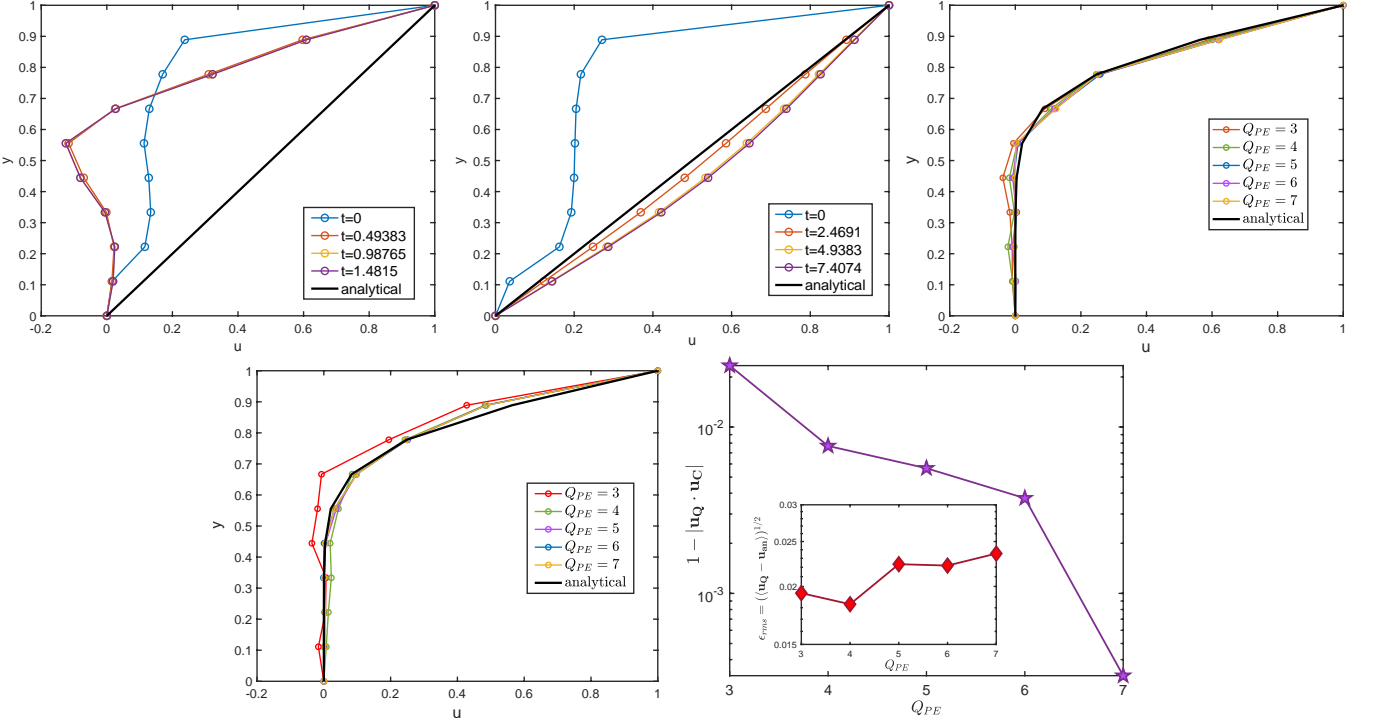


FIG. 6: (a) and (b) shows the quantum simulation of the flow field evolving forward in time towards steady state (analytical solution shown as solid black line) using BE scheme that use 7 and 12 qubits (3 and 8 QPE qubits (Q_{PE}), respectively), with $\mathbf{u}(\mathbf{y}, 0) = 0$, $N = 10$, $Re = 10$, $\partial p / \partial x = 0$ and $dt = 0.01$. The accuracy of the converged solution improves for higher Q_{PE} similar to the Poiseuille flow case. Here the velocity field is solved for at every time step; (c) shows increasingly accurate converged solutions with increasing Q_{PE} , but solved using the FE scheme where the velocity field is solved for all time steps in one shot, and only the final solution is extracted. Here $\alpha = 0.5$ is set to meet the von Neumann stability criterion and the parameter $T_0^* = 5.0$ is fixed. It is important to note that, the same T_0^* works for both Poiseuille flow and Couette flow independent of the boundary conditions, since it depends only on κ and form of the matrix. (d) shows the one-shot method, but it is solved with a BE scheme for $T_0^* = 6.5$. (e) shows both (1-fidelity) and ϵ_{rms} (inset) with increasing Q_{PE} from 3 to 7 computed for the one-shot FE case.

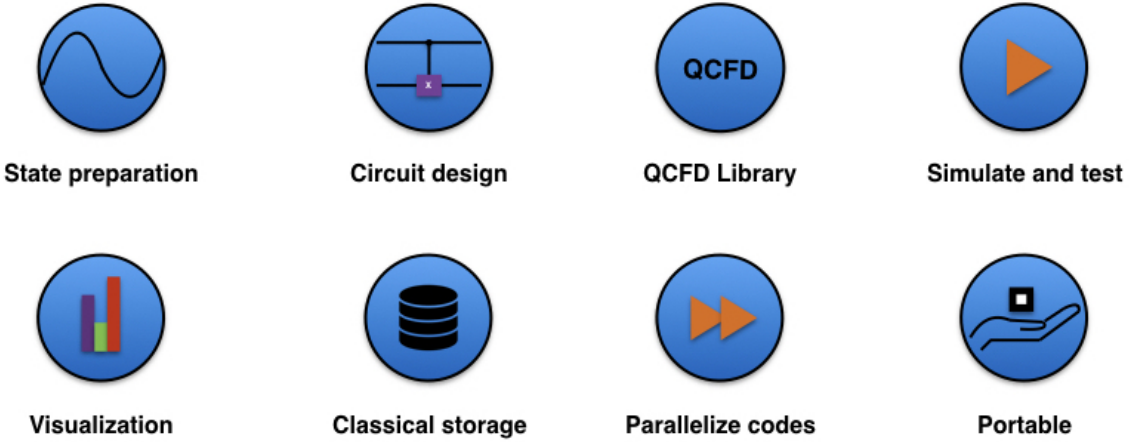


FIG. 7: Overview of the QFlowS features

Appendix C: Quantum State Preparation

QFlowS is equipped with a Quantum State Preparation (QSP) library that includes algorithms that cor-

respond to certain classes of states with specific properties. We briefly elucidate two such algorithms used here. When the state that is being initialized on a quantum

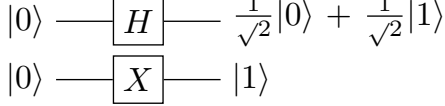


FIG. 8: 2 qubit circuit

$$U = H_1 \otimes X_0 = \frac{1}{\sqrt{2}} \begin{bmatrix} 0 & 1 & 0 & 1 \\ 1 & 0 & 1 & 0 \\ 0 & 1 & 0 & -1 \\ 1 & 0 & -1 & 0 \end{bmatrix} \Rightarrow \begin{bmatrix} u_0 \\ u_1 \\ u_2 \\ u_3 \end{bmatrix} \mapsto \frac{1}{\sqrt{2}} \begin{bmatrix} u_1 + u_3 \\ u_0 + u_2 \\ u_1 - u_3 \\ u_0 - u_2 \end{bmatrix} \quad (B2)$$

tum computer has a specific functional form such as log-concavity, it is known that it can be prepared efficiently [32, 38, 40, 41]. The original algorithm proposed in [38] proceeds as follows. Consider an arbitrary n-qubit initial state given by

$$|\psi\rangle = \sum_{i=0}^{2^n-1} \sqrt{p_i} |i\rangle, \quad (C1)$$

where p_i is the i -th region of discretely sampled elements/regions from a log-concave probability distribution function $p(\omega)$. With the existence of an efficient classical subroutine to perform partial sums given by

$$p_i = \int_{\omega_L^i}^{\omega_R^i} p_\omega d\omega, \quad p_{iL} = \int_{\omega_L^i}^{(\omega_R^i - \omega_L^i)/2} p_\omega d\omega, \quad (C2)$$

where p_i and p_{iL} are probabilities of the point lying in the entire region i and the left half of the region i , respectively, we can construct a circuit that prepares an n-qubit state for $k < m$ as

$$|\psi^{(k)}\rangle = \sum_{i=0}^{2^k-1} \sqrt{p_i^{(k)}} |i\rangle. \quad (C3)$$

Now we can further discretize this to yield the state

$$|\psi^{(k+1)}\rangle = \sum_{i=0}^{2^{k+1}-1} \sqrt{p_i^{(k+1)}} |i\rangle \quad (C4)$$

by the following steps. Given the ability to compute the quantities in eq. C2, we can compute the conditional probability function $f_k(i)$

$$f_k(i) = \frac{p_{iL}}{p_i}. \quad (C5)$$

With this we now compute the next level of discretization by constructing a quantum arithmetic circuit that performs

$$|i\rangle|0\rangle \mapsto |i\rangle|\theta_i\rangle, \quad (C6)$$

where $\theta_i = \arccos(\sqrt{f_k(i)})$. Further, by adding an ancillary qubit (($k+1$)-th qubit) we perform controlled $R_y(\theta_i)$ rotation gates (controlled on θ); uncomputing the second register we get

$$\begin{aligned} \sqrt{p_i^{(k+1)}} |i\rangle|\theta_i\rangle|0\rangle &\mapsto \sqrt{p_i^{(k)}} |i\rangle|\theta_i\rangle(\cos \theta_i |0\rangle + \sin \theta_i |1\rangle) \\ &\equiv \sum_{i=0}^{2^{k+1}-1} \sqrt{p_i^{(k+1)}} |i\rangle = |\psi^{(k+1)}\rangle. \end{aligned} \quad (C7)$$

Now repeat this $\mathcal{O}(n)$ times to generate an n -qubit state with the distribution sampled over 2^n regions. Though the complexity of such a method could be seen as $\mathcal{O}(n)$, the quantum arithmetic circuits are generally expensive and hence one could alternatively follow an improvement as proposed in [50]. To construct a circuit based on the above method described here, we employ the binary tree formulation as shown in [41], which we shall call **QSP-1**. Let us consider loading 4 arbitrary non-zero values onto a 2 qubit state as

$$|\psi\rangle = u_0|00\rangle + u_1|01\rangle + u_2|10\rangle + u_3|11\rangle. \quad (C8)$$

To construct the circuit with QSP-1, we create a binary tree as shown on the left panel of figure 9(a), where we start with the values to be loaded as the terminal nodes at the base of the tree. These values are pairwise squared (since probabilities are squares of amplitudes) and summed to build the tree upwards. Finally, all nodes should converge to 1, as one should expect. Now, to prepare the quantum states, we traverse the tree downwards starting from the vertex, which corresponds to the initial state $|\psi\rangle = |0\rangle \otimes |0\rangle$. Every node has two children: the zero-child and the one-child which have amplitudes corresponding to either the $|0\rangle$ or $|1\rangle$ state, respectively. Then we compute at every node, the angle $\theta = \arccos(\sqrt{\frac{\text{zero-child}}{\text{one-child}}})$ and apply a controlled $R_y(\theta)$ gate, where the control sequence is the bit sequence of the corresponding node. In the example shown in figure S4, to compute θ_2 , we look at the two children and obtain 0.25(zero-child) and 0.5(one-child). Therefore $\theta_2 = \arccos(\sqrt{\frac{0.25}{0.5}}) = \pi/4$. Here the parent node, 0.75 corresponds to a zero-child branch. So the controlled- R_y gate will operate when qubit 1 is set to 0. Thus, after $R_y(\theta_1)$ we get $\sqrt{0.75}|0\rangle + \sqrt{0.25}|1\rangle \otimes |0\rangle$. Further with successive applications of controlled gates $R_y(\theta_2)$ and $R_y(\theta_3)$ we obtain

$$|0\rangle \otimes |0\rangle \xrightarrow{R_y(\theta_1)} \sqrt{0.75}|0\rangle + \sqrt{0.25}|1\rangle \otimes |0\rangle \quad (C9)$$

$$\begin{aligned} & \sqrt{0.75}|0\rangle + \sqrt{0.25}|1\rangle) \otimes |0\rangle \xrightarrow{R_y(\theta_2), R_y(\theta_3)} \\ & \sqrt{0.25}|00\rangle + \sqrt{0.5}|01\rangle + \sqrt{0.125}|10\rangle + \sqrt{0.125}|11\rangle. \end{aligned} \quad (\text{C10})$$

The corresponding quantum circuit for QSP-1 is shown in the left panel of figure 9(b). Now notice that such a method has a total of $\mathcal{O}(n)$ stages which is logarithmic in the size of the state vector. Methods based on [38] will work best when the input velocity field to be loaded has a log-concave form. However, when we look at the gate complexity of the number of CNOTs, it grows exponentially as $\mathcal{O}(2^n)$. To ameliorate this, we employ **QSP-2**, which drastically reduces the CNOT gate count by $\geq 90\%$; but this is true for sparse quantum states and is based on the method proposed in [43, 51]. In fact, this condition works in our favor for the linear solvers considered here. Firstly, we know that between the two time-stepping schemes used in this work, one shot FE and BE schemes are more accurate and efficient since it does not need of repeated measurements and state preparation at every time step. The right hand side of the equation in that approach can be readily seen to be a sparse vector; importantly, we consider here all the quantum registers including ancilla qubits to be one single sparse state that needs to be prepared. For flow problems and system sizes considered here, this provides an initial sparse quantum state with N_{nz} non-zero elements, where $N_{nz} \in [n, 5n]$ with an improvement in CNOT count as high as $\approx 94\%$. Further unlike other state preparation algorithms which require exponentially large number of ancillary qubits, this method requires only one. To implement such a circuit, we consider the same 4 values but now loaded onto a 4 qubit state to make it sparse ($N_{nz} = n$). Again we construct a tree called as a *Decision Diagram (DD)* [43] as shown in the right panel of figure 9(a). The tree is constructed such that q_1 through q_4 depict the different qubits $|q_1 q_2 q_3 q_4\rangle$. The solid and dashed arrows/edges denotes whether that specific parent node evaluates a 0 or 1, and points to the corresponding zero-child or one-child. For instance, the left-most branch of QSP-2 in figure 9(a) has the sequence of solid-solid-dashed-solid lines, corresponding to the state $|1101\rangle$. However, owing to possible redundant connections one can sometimes invoke reduction rules [43] to simplify the DD by eliminating a few nodes; for instance, the right-most node with q_3 can be simplified as shown, since both children at the terminal nodes point to the same value. Thus by following the rules as detailed in [43], one can generate an efficient circuit with minimal CNOT gates as shown in fig. 9(b) (right panel), which is of the order $k \times \mathcal{O}(n) \ll \mathcal{O}(2^n)$, where k is the number of paths $\leq N_{nz}$ in the DD, whereas the time complexity is $\mathcal{O}(2kn)$. This procedure drastically reduces the number of CNOT gates thus making it more amenable for implementation on near-term QCs.

Appendix D: Quantum Post Processing

In this section we outline the Quantum Post Processing (QPP) protocol for computing the viscous dissipation rate per unit volume $\varepsilon = \nu \langle (\frac{\partial u}{\partial y})^2 \rangle$. The method proposed here is versatile, making it applicable to more general nonlinear quantities as well. In brief, to compute the above quantity we would first need to take the derivative of the velocity field with respect to the wall-normal direction $\partial u / \partial y$, for which we employ the well-known spectral method as discussed in Section 4.A. Further, for computing the square of that quantity (or any nonlinear function) we first invoke the Quantum Analog-Digital Converter (QADC-QDAC)[47] to convert the representation of the derivatives into binary format and then perform either quantum arithmetic or direct controlled rotation operations to finally yield the squares of the derivatives in amplitude-encoding format, after undoing the QADC operation outlined in Section 4.B.

1. Velocity gradients - spectral method

Computing derivatives in spectral space instead of real space is tantamount to simple scalar multiplication of vector elements by corresponding wave-vectors k . Let us consider the following n-qubit state resulting from a QLSA solution

$$|\phi\rangle = \sum_{j=0}^{N_g-1} u_j |j\rangle. \quad (\text{D1})$$

where u_i are the velocities at different grid points. First, we apply the Inverse Discrete Fourier Transform (IDFT), which in the quantum setting is the IQFT, to transition into spectral space as

$$U_{IQFT} |\phi\rangle \mapsto \frac{1}{\sqrt{N}} \sum_{k=0}^{k=N_g} e^{-2\pi i \frac{jk}{N_g}} |k\rangle. \quad (\text{D2})$$

Next we multiply the state by a constant diagonal matrix Λ defined as,

$$\Lambda_{kk} = \begin{cases} 2\pi ik, & k \in [0, N_g/2 - 1] \\ 0, & k = N_g/2 \\ 2\pi i(k - N_g), & k \in [N_g/2 + 1, N_g - 1] \end{cases} \quad (\text{D3})$$

and perform the QFT (given by the kernel $e^{2\pi i \frac{jk}{N_g}}$) to transform back, which yields a final state that gives the derivative in real space ($u' = \partial u / \partial y$) as

$$|\phi'\rangle = U_{IQFT} \Lambda U_{QFT} |\phi\rangle = \sum_{j=0}^{N_g-1} \frac{du_j}{dy} |j\rangle \equiv \sum_{j=0}^{N_g-1} u'_j |j\rangle \quad (\text{D4})$$

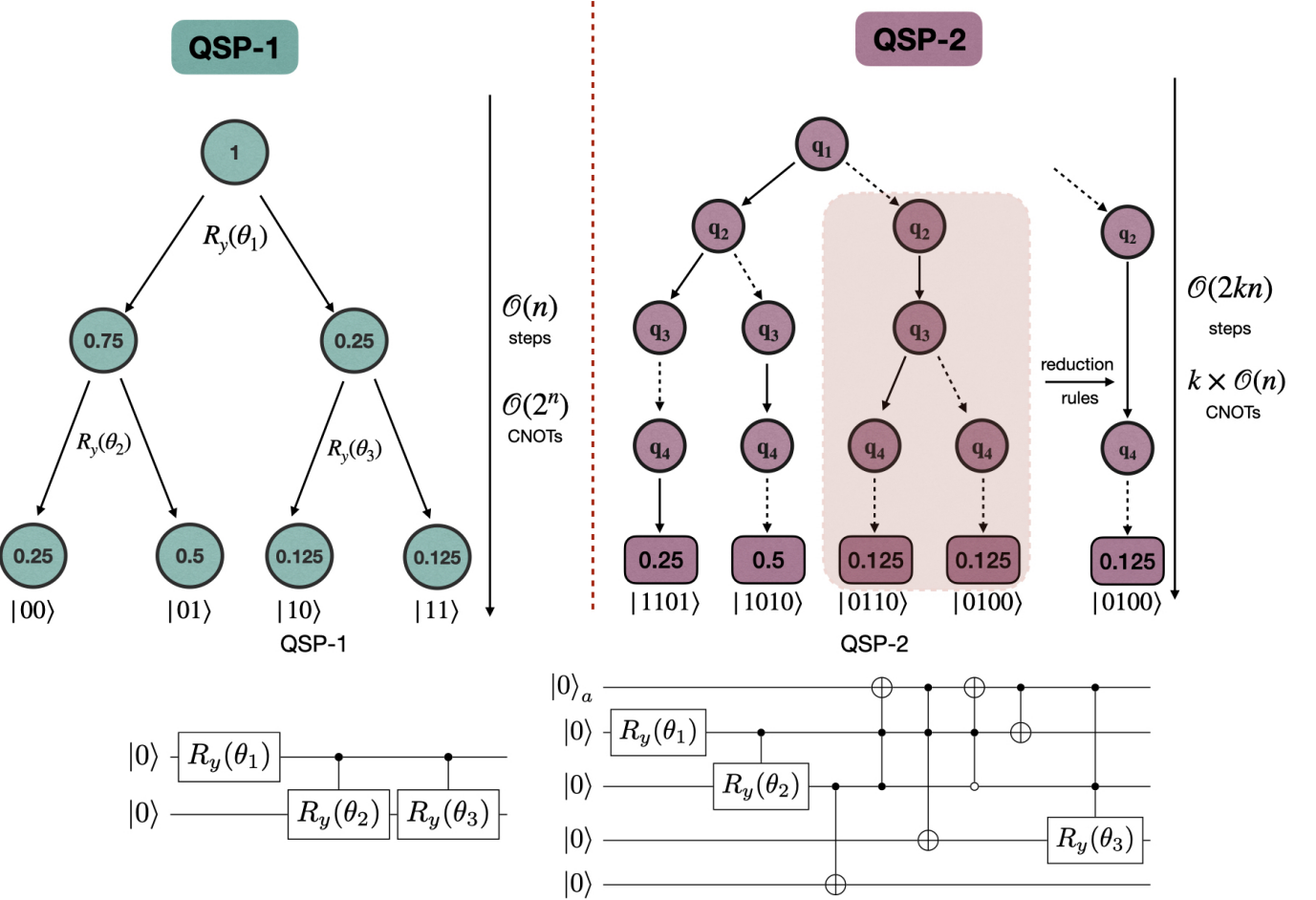


FIG. 9: (a) Computing the Decision Trees for QSP -1,2 (b) Quantum circuits for QSP -1 and -2 corresponding (a) to load four real values

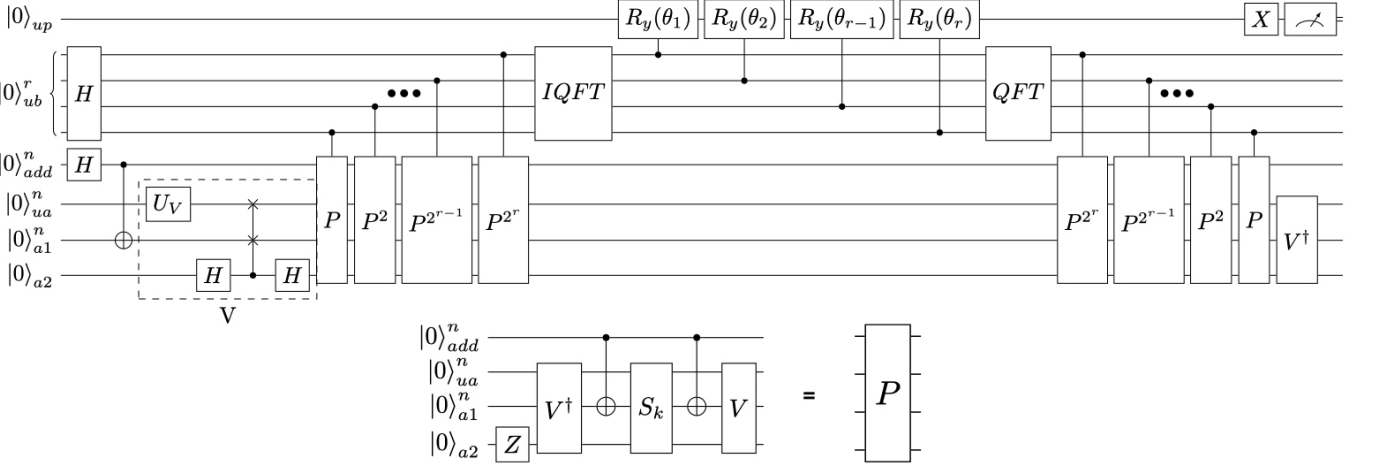


FIG. 10: Quantum Post Processing (QPP) circuit

2. Nonlinear transform

The final step in computing the dissipation involves computing the squares of the velocity gradients that re-

quires a nonlinear transformation of the quantum amplitudes. Consider a velocity gradient state vector prepared by an oracle U_V as shown in figure 1.a in the main text, which either results from a direct quantum state

preparation algorithm or the QLSA itself. Our aim is to implement the mapping

$$|\zeta\rangle = \sum_{k=0}^{N_g-1} u'_k |k\rangle \mapsto \sum_{k=0}^{N_g-1} (u'_k)^2 |k\rangle. \quad (\text{D5})$$

This requires a total of 6 quantum registers as shown in figure 10, where q_{up} is an ancillary qubit to store the amplitude encoding of $(u')^2$, q_{ub} stores the r -bit basis encoding of u' , q_{add} is the address register, q_{ua} encodes the input amplitude encoding of u and q_{a1}, q_{a2} are ancillary qubits. Here, we implement a modified version of the Quantum Analog Digital Converter described in [47]. The steps are as follows:

1. STEP 1: Generate the basis superposition for the address qubits by applying Hadamard gates on q_{add} register to yield $\frac{1}{\sqrt{N}} \sum_{s=0}^{N_{add}-1} |s\rangle_{add}$. Following this, we apply CNOT gate on q_{a1} to clone the basis of the address register.

2. STEP 2: We then load the velocity derivative values into q_{ua} by the oracle U_V , which gives $\frac{1}{\sqrt{N}} \sum_s \sum_c u'_c |s\rangle_{add} |c\rangle_{ua} |s\rangle_{a1}$.

3. STEP 3: Since we are interested finally in a squared quantity we can extract simply the absolute value of u' by using the SWAP test circuit (denoted by the portion of circuit enclosed in the dotted box V in figure 10, excluding U_V). This is a procedure for comparing two states to determine their closeness by estimating the inner product. The SWAP test of two state $|\phi_1\rangle$ and $|\phi_2\rangle$ yields a quantity of the type $\frac{1}{2}(1 - |\langle\phi_1|\phi_2\rangle|)$. Here we use the test without any measurements, which gives us absolute values of u' . This leaves us with

$$= \sum_s \frac{1}{2\sqrt{N}} |k\rangle_{add} \left[\underbrace{\left(\sum_c u'_c |c\rangle_{ua} |s\rangle_{a1} + |s\rangle_{ua} \sum_c u'_c |c\rangle_{a1} \right)}_{\zeta_{s0}} \right] |0\rangle_{a2} \quad (\text{D6})$$

$$+ \underbrace{\left(\sum_c u'_c |c\rangle_{ua} |s\rangle_{a1} - |s\rangle_{ua} \sum_c u'_c |c\rangle_{a1} \right)}_{\zeta_{s1}} |1\rangle_{a2} \\ = \sum_s \frac{1}{\sqrt{N}} |k\rangle_{add} \left[\alpha_{s0} |\zeta_{s0}\rangle |0\rangle_{a2} + \alpha_{s1} |\zeta_{s1}\rangle |1\rangle_{a2} \right] \quad (\text{D7})$$

4. STEP 4: We now perform Quantum Phase Estimation with a gate P defined as shown in fig. 10 (bottom panel), where $S_k = \mathcal{I} - 2(|0\rangle\langle 0|)_{ua,a2} \otimes (|s\rangle\langle s|)_{a1}$, this being a conditional phase shift operator. The details of this step can be found in [43]. The QPE along with the IQFT results in the state

$$|\zeta\rangle_{ub,ua,a1,a2} = \frac{1}{\sqrt{2N}} \sum_s |s\rangle_{add} (|\beta\rangle_{ub} |\zeta_+\rangle + |(1-\beta)\rangle_{ub} |\zeta_-\rangle), \quad (\text{D8})$$

where $\sin(\pi\beta) = \sqrt{0.5(1 + (u'_c)^2)}$ is stored as an r -bit basis representation, and $\zeta_{\pm} = \frac{1}{\sqrt{2}} (|\zeta_{s0}\rangle \pm i|\zeta_{s1}\rangle)$ form the eigen-basis of P .

5. STEP 5: Now, instead of performing quantum arithmetic as shown in [47], we can directly compute the squares of u'_c and transform back to amplitude encoding together by applying conditional rotation operators. We introduce another ancillary qubit q_{up} and apply $R_y(\theta_r)$ operators on it (for a given $c = r$), conditioned on the q_{up} qubits, where $\theta = 2\gamma$. Since $u'_r = \sqrt{2\sin^2 \pi\gamma_r - 1}$, therefore $\sin(2\gamma_r) = (u'_r)^2$. Thus $R_y(\theta_r)$ performs the operation, $|0\rangle_{up} \mapsto (\sqrt{(1 - (u'_r)^4)}|0\rangle + (u'_r)^2|1\rangle)$. For a given r -basis, these values of θ can be hard encoded into the circuit. Following this step, we undo the operations on q_{ua} , q_{a1} and q_{a2} to set them to $|0\rangle$, which yields the final state

$$R \sum_{c=0}^N \left(\sqrt{(1 - (u'_c)^4)} |0\rangle_{up} + (u'_c)^2 |1\rangle_{up} \right) |c\rangle_{add} |0\rangle_{ub,ua,a1,a2}. \quad (\text{D9})$$

When measured in the computational basis after applying X gate, this gives

$$R' \sum_{c=0}^N (u'_c)^2 |0\rangle_{up} |c\rangle_{add} |0\rangle_{ub,ua,a1,a2}, \quad (\text{D10})$$

where R and R' are corresponding normalization constants. The above equation is the transformation we sought in eq. D5. Given an n -qubit state such as $|\psi\rangle^n = \sum_p w_p |p\rangle$, we can compute the sum of all amplitudes by applying $U_{avg} = H^{\otimes n}$ which gives $w_0 = \sum_p w_p$. Using this we can compute the sum of $\sum_c (u'_c)^2$ and finally measure the first qubit basis state with this value. Of course, we would need to post-multiply it by corresponding normalization constants to retrieve the right solution; importantly, we have to divide the final solution by 2, since we know that $\sin(2\pi\gamma) = \sin(2\pi(1 - \gamma))$. From eq. D8 we observe that we will get repeated values when we transform into amplitude encoding. Further, we multiply classically with the appropriate viscosity ν and divide the solution by the number of grid points to yield the final dissipation rate,

$$\varepsilon = \nu \langle \left(\frac{\partial u}{\partial y} \right)^2 \rangle. \quad (\text{D11})$$

The complexity of the above QPP is as follows: (a) STEPS 1-3 require $\mathcal{O}(\log_2 N)$ gates; (b) STEP 4 has single and two qubit gates with a complexity of $\mathcal{O}((\log_2 N)^2/\epsilon_{QPP})$ along with $\mathcal{O}(1/\epsilon_{QPP})$ calls to U_V ; (c) STEP 5, which uses controlled rotations has the complexity $\mathcal{O}(1/\epsilon_{QPP})$. Thus, the overall complexity of $\mathcal{O}((\log_2 N)^2/\epsilon_{QPP})$. U_V is either the QLSA itself or, if the form of the velocity field is known, it can be prepared by QSP-1,2 thus amounting to a complexity of $\mathcal{O}(U_V) =$

$\min\{\mathcal{O}(\text{poly log}(N/\epsilon)\kappa/\epsilon_{QPP}), \mathcal{O}(n), \mathcal{O}(kn)\}$. The complexity of the entire algorithm presented in this work is summarized in Table I (where $n = \log_2(N)$). We caution the readers that these complexities are only estimates and warrant a more detailed analysis of the space, time and gate complexity of the algorithms presented here.

TABLE I: Summary of time complexity of quantum subroutines

Quantum subroutine	Complexity
QSP-1	$\mathcal{O}(n)$
QSP-2	$\mathcal{O}(2kn)$
QLSA-1	$\mathcal{O}(\text{poly log}(N)s^2\kappa^2/\epsilon)$
QLSA-2	$\mathcal{O}(\text{poly log}(N/\epsilon)\kappa)$
QPP	$\mathcal{O}(U_V) + \mathcal{O}((\log N)^2/\epsilon_{QPP})$
End-to-end	$\min\{\mathcal{O}(\text{poly log}(N/\epsilon)\kappa/\epsilon_{QPP}), \mathcal{O}(kn/\epsilon_{QPP})\}$ $+ \mathcal{O}((\log N)^2/\epsilon_{QPP})\}$ $\approx \mathcal{O}(\text{poly log}(N/\epsilon)\kappa/\epsilon_{QPP})$

-
- [1] K. P. Iyer, J. D. Scheel, J. Schumacher, and K. R. Sreenivasan, Classical 1/3 scaling of convection holds up to $Ra = 10^{15}$, Proc. Nat. Acad. Sci. **117**, 7594 (2020).
- [2] P. K. Yeung and K. Ravikumar, Advancing understanding of turbulence through extreme-scale computation: Intermittency and simulations at large problem sizes, Phys. Rev. Fluids **5**, 110517 (2020).
- [3] P.-K. Yeung, K. Ravikumar, and S. Nichols, Turbulence simulations on the verge of exascale: Gpu algorithms and an alternative to long simulations at high resolutions, Bull. Am. Phys. Soc., Q49.004 (2022).
- [4] J. S. Rood, M. T. Henry de Frahan, M. S. Day, H. Sitaran, S. Yellapantula, B. A. Perry, R. W. Grout, A. Almgren, W. Zhang, and J. Chen, *Enabling Combustion Science Simulations for Future Exascale Machines*, Tech. Rep. (National Renewable Energy Lab. (NREL), Golden, CO, 2021).
- [5] K. P. Iyer, S. S. Bharadwaj, and K. R. Sreenivasan, The area rule for circulation in three-dimensional turbulence, Proc. Nat. Acad. Sci. **118** (2021).
- [6] D. Buaria and K. R. Sreenivasan, Scaling of acceleration statistics in high Reynolds number turbulence, Phys. Rev. Lett. **128**, 234502 (2022).
- [7] G. Bell, D. H. Bailey, J. Dongarra, A. H. Karp, and K. Walsh, A look back on 30 years of the gordon bell prize, J. High Perform. Comput. Appl. **31**, 469 (2017).
- [8] M. A. Nielsen and I. L. Chuang, *Quantum Computation and Quantum Information: 10th Anniversary Edition* (Cambridge University Press, 2010).
- [9] S. Jordan, Quantum algorithm zoo, <https://quantumalgorithmzoo.org/> (2022).
- [10] D. D. Awschalom, H. Bernien, R. Brown, A. Clerk, E. Chitambar, A. Dibos, J. Dionne, M. Eriksson, B. Fefferman, G. D. Fuchs, *et al.*, *A Roadmap for Quantum Interconnects*, Tech. Rep. (Argonne National Lab.(ANL), Argonne, IL (United States), 2022).
- [11] Y. Alexeev, D. Bacon, K. R. Brown, R. Calderbank, L. D. Carr, F. T. Chong, B. DeMarco, D. Englund, E. Farhi, B. Fefferman, A. V. Gorshkov, A. Houck, J. Kim, S. Kimmel, M. Lange, S. Lloyd, M. D. Lukin, D. Maslov, P. Maunz, C. Monroe, J. Preskill, M. Roetteler, M. J. Savage, and J. Thompson, Quantum computer systems for scientific discovery, PRX Quantum **2**, 017001 (2021).
- [12] S. S. Bharadwaj and K. R. Sreenivasan, Quantum computation of fluid dynamics, Ind. Acad. Sci. Conf. Ser. **3**, 77 (2020).
- [13] J.-P. Liu, H. Ø. Kolden, H. K. Krovi, N. F. Loureiro, K. Trivisa, and A. M. Childs, Efficient quantum algorithm for dissipative nonlinear differential equations, Proc. Nat. Acad. Sci. **118** (2021).
- [14] Y. T. Lin, R. B. Lowrie, D. Aslangil, Y. Subaşı, and A. T. Sornborger, Koopman von Neumann mechanics and the Koopman representation: A perspective on solving nonlinear dynamical systems with quantum computers, arXiv:2202.02188 (2022).
- [15] D. Giannakis, A. Ourmazd, P. Pfeffer, J. Schumacher, and J. Slawinska, Embedding classical dynamics in a quantum computer, Phys. Rev. A **105**, 052404 (2022).
- [16] By this we mean an algorithm that efficiently prepares a quantum state, processes it and outputs a result by measurement while retaining all or some net quantum advantage.
- [17] A. M. Childs, J.-P. Liu, and A. Ostrander, High-precision quantum algorithms for partial differential equations, Quantum **5**, 574 (2021).
- [18] G. T. Balducci, B. Chen, M. Möller, M. Gerritsma, and R. De Breuker, Review and perspectives in quantum computing for partial differential equations in structural mechanics, Frontiers in Mechanical Engineering, 75 (2022).
- [19] F. Y. Leong, W.-B. Ewe, and D. E. Koh, Variational quantum evolution equation solver, Sci. Rep. **12**, 10817 (2022).
- [20] M. Lubasch, J. Joo, P. Moinier, M. Kiffner, and D. Jaksch, Variational quantum algorithms for nonlinear problems, Phys. Rev. A **101**, 010301 (2020).
- [21] F. Gaitan, Finding flows of a Navier–Stokes fluid through quantum computing, npj Quantum Information **6**, 61 (2020).
- [22] F. Oz, O. San, and K. Kara, An efficient quantum partial differential equation solver with chebyshev points, Sci. Rep. **13**, 7767 (2023).
- [23] N. Gourianov, M. Lubasch, S. Dolgov, Q. Y. van den Berg, H. Babaee, P. Givi, M. Kiffner, and D. Jaksch, A quantum-inspired approach to exploit turbulence structures, Nat. Comput. Sci. **2**, 30 (2022).
- [24] A. W. Harrow, A. Hassidim, and S. Lloyd, Quantum algorithm for linear systems of equations, Phys. Rev. Lett. **103**, 150502 (2009).
- [25] A. M. Childs, R. Kothari, and R. D. Somma, Quantum algorithm for systems of linear equations with exponentially improved dependence on precision, SIAM Journal Computing **46**, 1920 (2017).

- [26] S. Aaronson, Read the fine print, *Nat. Phys.* **11**, 291 (2015).
- [27] Y. Cao, A. Papageorgiou, I. Petras, J. Traub, and S. Kais, Quantum algorithm and circuit design solving the poisson equation, *New. J. Phys.* **15**, 013021 (2013).
- [28] A. Montanaro and S. Pallister, Quantum algorithms and the finite element method, *Phys. Rev. A* **93**, 032324 (2016).
- [29] Quantiki, List of quantum simulators, <https://quantiki.org/wiki/list-qc-simulators> (2023).
- [30] A. S. Green, P. L. Lumsdaine, N. J. Ross, P. Selinger, and B. Valiron, Quipper: a scalable quantum programming language, in *Proceedings of the 34th ACM SIGPLAN Conference on Programming Language Design and Implementation* (2013) pp. 333–342.
- [31] T. Jones, A. Brown, I. Bush, and S. C. Benjamin, Quest and high performance simulation of quantum computers, *Sci. Rep.* **9**, 1 (2019).
- [32] A. C. Vazquez and S. Woerner, Efficient state preparation for quantum amplitude estimation, *Phys. Rev. Appl.* **15**, 034027 (2021).
- [33] V. Giovannetti, S. Lloyd, and L. Maccone, Architectures for a quantum random access memory, *Phys. Rev. A* **78**, 052310 (2008).
- [34] I. M. Georgescu, S. Ashhab, and F. Nori, Quantum simulation, *Rev. Mod. Phys.* **86**, 153 (2014).
- [35] D. W. Berry, A. M. Childs, R. Cleve, R. Kothari, and R. D. Somma, Exponential improvement in precision for simulating sparse hamiltonians, in *Proceedings of the Forty-Sixth Annual ACM Symposium on Theory of Computing* (2014) pp. 283–292.
- [36] D. W. Berry, A. M. Childs, and R. Kothari, Hamiltonian simulation with nearly optimal dependence on all parameters, in *2015 IEEE 56th Annual Symposium on Foundations of Computer Science* (IEEE, 2015) pp. 792–809.
- [37] A. Ambainis, Variable time amplitude amplification and a faster quantum algorithm for solving systems of linear equations, [arXiv:1010.4458](https://arxiv.org/abs/1010.4458) (2010).
- [38] L. Grover and T. Rudolph, Creating superpositions that correspond to efficiently integrable probability distributions, [arXiv:quant-ph/0208112](https://arxiv.org/abs/quant-ph/0208112) (2002).
- [39] A. G. Rattew and B. Koczor, Preparing arbitrary continuous functions in quantum registers with logarithmic complexity, [arXiv:2205.00519](https://arxiv.org/abs/2205.00519) (2022).
- [40] A. C. Vazquez, R. Hiptmair, and S. Woerner, Enhancing the quantum linear systems algorithm using Richardson extrapolation, *ACM Trans. Quantum Comput.* **3**, 1 (2022).
- [41] A. Prakash, *Quantum algorithms for linear algebra and machine learning. PhD Thesis (University of California, Berkeley)* (2014).
- [42] P. Pfeffer, F. Heyder, and J. Schumacher, Hybrid quantum-classical reservoir computing of thermal convection flow, *Phys. Rev. Research* **4**, 033176 (2022).
- [43] F. Mozafari, G. De Micheli, and Y. Yang, Efficient deterministic preparation of quantum states using decision diagrams, *Phys. Rev. A* **106**, 022617 (2022).
- [44] H. Wolkowicz and G. P. Stylian, More bounds for eigenvalues using traces, *Linear Algebra Appl.* **31**, 1 (1980).
- [45] A. Scherer, B. Valiron, S.-C. Mau, S. Alexander, E. Van den Berg, and T. E. Chapuran, Concrete resource analysis of the quantum linear-system algorithm used to compute the electromagnetic scattering cross section of a 2d target, *Quantum Inf. Process.* **16**, 1 (2017).
- [46] G. Brassard, P. Hoyer, M. Mosca, and A. Tapp, Quantum amplitude amplification and estimation, *Contemporary Mathematics* **305**, 53 (2002).
- [47] K. Mitarai, M. Kitagawa, and K. Fujii, Quantum analog-digital conversion, *Phys. Rev. A* **99**, 012301 (2019).
- [48] S. Wang, Z. Wang, W. Li, L. Fan, G. Cui, Z. Wei, and Y. Gu, Quantum circuits design for evaluating transcendental functions based on a function-value binary expansion method, *Quantum Inf. Process.* **19**, 1 (2020).
- [49] Y. Subasi, R. D. Somma, and D. Orsucci, Quantum algorithms for systems of linear equations inspired by adiabatic quantum computing, *Phys. Rev. Lett.* **122**, 060504 (2019).
- [50] Y. R. Sanders, G. H. Low, A. Scherer, and D. W. Berry, Black-box quantum state preparation without arithmetic, *Phys. Rev. Lett.* **122**, 020502 (2019).
- [51] ANGEL, GITHUB REPOSITORY <https://github.com/fmozafari/angel> (2022).